Long noncoding RNAs emerge from transposon-derived antisense sequences and may contribute to infection stage-specific transposon regulation in a fungal phytopathogen

Jiangzhao Qian[1], Heba M. M. Ibrahim[2], Myriam Erz[1], Florian Kümmel[1,3], Ralph Panstruga[1], Stefan Kusch[1,*]

[1] Unit of Plant Molecular Cell Biology, Institute for Biology I, RWTH Aachen University, Worringerweg 1, D-52056 Aachen, Germany

[2] Division of Plant Biotechnics, Department of Biosystems, Faculty of Bioscience Engineering, Katholieke Universiteit Leuven, 3001 Leuven, Belgium

[3] current address: Department of Plant-Microbe Interactions, Max Planck Institute for Plant Breeding Research, Carl-von-Linné-Weg 10, Cologne D-50829, Germany

*** Corresponding author:**
Stefan Kusch, +49 241 80 26640, skusch@bio1.rwth-aachen.de

Abstract

The genome of the obligate biotrophic phytopathogenic barley powdery mildew fungus *Blumeria hordei* is inflated due to highly abundant and possibly active transposable elements (TEs). In the absence of the otherwise common repeat-induced point mutation transposon defense mechanism, noncoding RNAs could be key for regulating the activity of TEs and coding genes during the pathogenic life cycle. We performed time-course whole-transcriptome shotgun sequencing (RNA-seq) of total RNA derived from infected barley leaf epidermis at various stages of fungal pathogenesis and observed significant transcript accumulation and time point-dependent regulation of TEs in *B. hordei*. Using a manually curated consensus database of 344 TEs, we discovered phased small RNAs mapping to 104 consensus transposons, suggesting that RNA interference contributes significantly to their regulation. Further, we identified 5,127 long noncoding RNAs (lncRNAs) genome-wide in *B. hordei*, of which 823 originated from the antisense strand of a TE. Co-expression network analysis of lncRNAs, TEs, and coding genes throughout the asexual life cycle of *B. hordei* points at extensive positive and negative co-regulation of lncRNAs, subsets of TEs and coding genes. Our work suggests that similar to mammals and plants, fungal lncRNAs support the dynamic modulation of transcript levels, including TEs, during pivotal stages of host infection. The lncRNAs may support transcriptional diversity and plasticity amid loss of coding genes in powdery mildew fungi and may give rise to novel regulatory elements and virulence peptides, thus representing key drivers of rapid evolutionary adaptation to promote pathogenicity and overcome host defense.

Keywords: *Blumeria*; Powdery mildew; RNA interference; Long noncoding RNA (lncRNA); Transposable element; Co-expression

49 **Abbreviations**

50

51 cv.	Cultivar
52 GO	Gene ontology
53 hpi	Hours post inoculation
54 KEGG	Kyoto Encyclopedia of Genes and Genomes
55 LINE	Long interspersed nuclear element
56 lncRNA	Long noncoding RNA
57 LTR	Long terminal repeat
58 mRNA	Messenger-RNA
59 NMDS	Non-metric multidimensional scaling
60 PC	Principal component
61 phasiRNA	Phased secondary small interfering RNAs
62 qRT-PCR	Quantitative reverse transcriptase polymerase chain reaction
63 RIP	Repeat-induced point mutation
64 RNAi	RNA interference
65 RPKM	Reads per kilobase of transcript per million mapped reads
66 SINE	Short interspersed nuclear element
67 sRNA	Small RNA
68 TE	Transposable element
69 TPM	Transcripts per million

70

Introduction

Transposable elements (TEs) are selfish genetic and typically repetitive elements in genomes. Autonomous TEs carry genes for self-replication, transposition, and DNA integration, allowing them to multiply and spread in host genomes, often leading to high copy numbers. They are classified into DNA transposons, spreading by excision from one and integration into another genomic location ("cut-and-paste" mechanism), and retrotransposons, which transcribe their sequence into an RNA transcript, which in turn is reverse-transcribed and then integrated as a new copy into the genome, frequently at a distant site (Wicker et al. 2007; Lanciano and Cristofari 2020). TEs can dramatically influence genome size in eukaryotes (Chénais et al. 2012), destabilize genome integrity (Chuong et al. 2017), and significantly affect genome structure and gene expression patterns (Slotkin and Martienssen 2007).

Powdery mildew fungi are ubiquitous phytopathogens of many plant species in temperate climates (Glawe 2008; Braun and Cook 2012). The genomes of powdery mildew fungi often consist to more than 50% of TEs, resulting in largely inflated genomes and highly variable genome sizes between species (Kusch, Qian, et al. 2023). The barley (*Hordeum vulgare*) powdery mildew *Blumeria hordei* possesses a genome of approximately 125 million base pairs (Mbp) in length with a TE content of more than 74% (Spanu et al. 2010; Frantzeskakis et al. 2018). The TE space of *B. hordei* is dominated by long interspersed nuclear element (LINE) elements, predominantly *Tad1*, and long terminal repeat (LTR) elements, especially *Ty3* (syn. "*Gypsy*") and *Copia* (Spanu et al. 2010; Frantzeskakis et al. 2018). While such a high TE content likely poses a stress on genome integrity in *B. hordei*, TEs can also be a source of variability and adaptation (Chuong et al. 2017) and contribute to the evolutionary invention of novel virulence factors (Nottensteiner et al. 2018; Sabelleck and Panstruga 2018). However, it is presently unknown how powdery mildew fungi regulate their TEs to prevent uncontrolled spread and, hence, genome disintegration.

Filamentous fungi evolved the repeat-induced point mutation (RIP) mechanism that serves to mutagenize repetitive sequences and helps to disable TEs (Gladyshev 2017). However, the RIP mechanism is missing in all powdery mildew fungi sequenced to date (Spanu et al. 2010; Frantzeskakis et al. 2018; Frantzeskakis et al. 2019; Kusch, Qian, et al. 2023), suggesting that it was lost in the course of evolution in a common ancestor of powdery mildew fungi (Frantzeskakis et al. 2019). Instead, we previously found that small RNAs (sRNAs) can originate from *B. hordei* TEs and that phased small RNAs (phasiRNAs) align to fungal TEs, suggesting frequent RNA interference (RNAi) to control TE activity (Kusch et al. 2018; Kusch, Singh, et al. 2023).

107 Long noncoding RNAs (lncRNAs) are transcripts longer than 200 nucleotides with no
108 apparent coding potential (Ulitsky and Bartel 2013; Quinn and Chang 2015). Like mRNAs,
109 lncRNAs are transcribed by RNA polymerase II and often processed by splicing,
110 7-methylguanosine capping, and polyadenylation (Zhang et al. 2019). lncRNAs can be
111 distinguished from sRNAs and microRNAs, which are smaller than 200 nucleotides (Bologna
112 and Voinnet 2014), RNA polymerase III-generated noncoding RNAs, including ribosomal and
113 transfer RNAs, and the RNA polymerase II-derived components of the spliceosome, i.e.
114 small nuclear RNAs (snRNAs) and small nucleolar RNAs (snoRNAs) (Mattick et al. 2023).
115 Compared to coding genes, lncRNAs frequently exhibit lower expression levels and
116 sequence conservation on average (Mattick et al. 2023). lncRNAs can be classified as
117 intergenic, intronic, sense, and antisense lncRNAs depending on their relative position to
118 coding genes (Zhao and Lin 2015), although the majority of lncRNAs described to date
119 reside in intergenic regions (Wang et al. 2018; Wang et al. 2019; Choi et al. 2022). lncRNAs
120 engage in biological processes such as transcriptional and post-transcriptional gene
121 regulation, epigenetic regulation, regulation of translation, and regulation of protein activity
122 (Kopp and Mendell 2018; Zhang et al. 2019). A number of lncRNAs have been functionally
123 analyzed in mammals, such as *HOTAIR, roX1, roX2*, and *Meg3*, which form triplexes with
124 purine-rich DNA regions to exert regulatory functions (Kalwa et al. 2016; Mattick et al. 2023),
125 and in plants, where lncRNAs are involved in developmental processes and stress
126 responses (Jampala et al. 2021). In fungi, lncRNAs function in regulating development,
127 stress and starvation responses, and pathogenic traits (Till, Mach, et al. 2018; Li et al. 2021).
128 For instance, the human-pathogenic fungus *Cryptococcus neoformans* exhibits dynamic
129 infection stress-related lncRNA expression patterns (Kalem and Panepinto 2022). The rice
130 blast fungus *Magnaporthe oryzae* expresses more than 500 lncRNAs specifically during
131 infection (Choi et al. 2022), suggesting that lncRNAs may be important for plant-pathogenic
132 fungi throughout host colonization. Interestingly, in maize, TEs can give rise to lncRNAs in
133 response to abiotic stresses (Lv et al. 2019), suggestive of regulatory roles exerted on TE
134 activity by lncRNAs. We hypothesize that lncRNAs could also occur in powdery mildew fungi,
135 be expressed during different infection stages, and fulfill regulatory functions toward
136 controlling TE activity.
137 In this work, we aimed to discover signs of co-regulation between TEs, coding genes, and
138 lncRNAs in the barley powdery mildew fungus *B. hordei*. We generated a time-course whole-
139 transcriptome shotgun transcriptome (RNA-seq) dataset to measure transcript levels at all
140 relevant stages of the asexual infection cycle of *B. hordei*, which allowed us to provide
141 manually curated high-quality genome-wide annotations of coding genes, TEs, and lncRNAs.
142 TEs exhibited signs of time point-specific regulation and co-regulation with mRNAs and
143 lncRNAs, and we found evidence for phasiRNAs linked to retrotransposons, suggestive of

144 RNAi-directed regulation of TEs in *B. hordei*. Importantly, we discovered 823 lncRNAs on the
145 antisense strand of TEs, which may provide precursors for RNAi with TEs.
146
147

148 Results

149

150 **Stranded total RNA sequencing of *B. hordei* and barley transcripts**
151 We hypothesize that *B. hordei* TEs are differentially regulated throughout the pathogenic life
152 cycle of the fungus. We inoculated the susceptible barley (*H. vulgare*) cultivar (cv.) 'Margret'
153 with *B. hordei* isolate $K1_{AC}$ (Barsoum et al. 2020) and procured total RNA from leaf epidermal
154 peelings (Li et al. 2019) in a time-course experiment. In three independent experimental
155 replicates per time-point, we sampled and performed stranded RNA-seq at 0, 6, 18, 24, 72,
156 and 120 hours post inoculation (hpi) to obtain transcriptomes of all major developmental
157 stages of the asexual pathogenic life cycle of *B. hordei* and its host, barley (**Figure 1A**). The
158 RNA sequencing (data available at NCBI/ENA/DDBJ under project accession
159 PRJNA835302) yielded on average 84,528,021 raw reads/sample and 81,708,016
160 reads/sample after quality trimming (**Supplementary Table 1**). FastQC quality control
161 revealed high per-base quality (per-base quality score > 30) across all samples, but also
162 7.7% sequence duplication on average, which originated from barley chloroplast RNA and
163 had no similarity to the *H. vulgare* and *B. hordei* nucleic genomes. Of the remaining reads,
164 0.2-1.5% and 4.6-24.8% mapped to the reference genome of *B. hordei* isolate DH14
165 (Frantzeskakis et al. 2018) at the early (0, 6, 18 and 24 hpi) and late (72 and 120 hpi) time
166 points, respectively. The relatively low fungal mapping percentage can be explained by the
167 *B. hordei* tissue only representing a small fraction of the biological sample material (leaf
168 epidermal peels), especially at early infection stages before 24 hpi. Further, between 65%
169 and 93% of the reads mapped to the *H. vulgare* cv. 'Morex' reference genome version
170 Morex3 (Mascher et al. 2021), while between 6.9% and 13.2% of the reads could neither be
171 assigned to the host nor the pathogen. Using Pearson correlation coefficient-based
172 hierarchical clustering, principal component (PC) analysis, and non-metric multidimensional
173 scaling (NMDS), we found that the sequencing samples from the same time points were
174 more similar to each other than to samples from the other time points (**Figure 1B-C**).
175 However, the principal components PC1 and PC2 did not separate *B. hordei* time points
176 6 hpi from 18 hpi, nor 72 hpi from 120 hpi, while hierarchical clustering and NMDS indicated
177 these to be different. Overall, both *B. hordei* and *H. vulgare* RNA-seq data clustered
178 according to infection time point, suggesting that the dataset is informative with respect to the
179 respective infection stage.
180

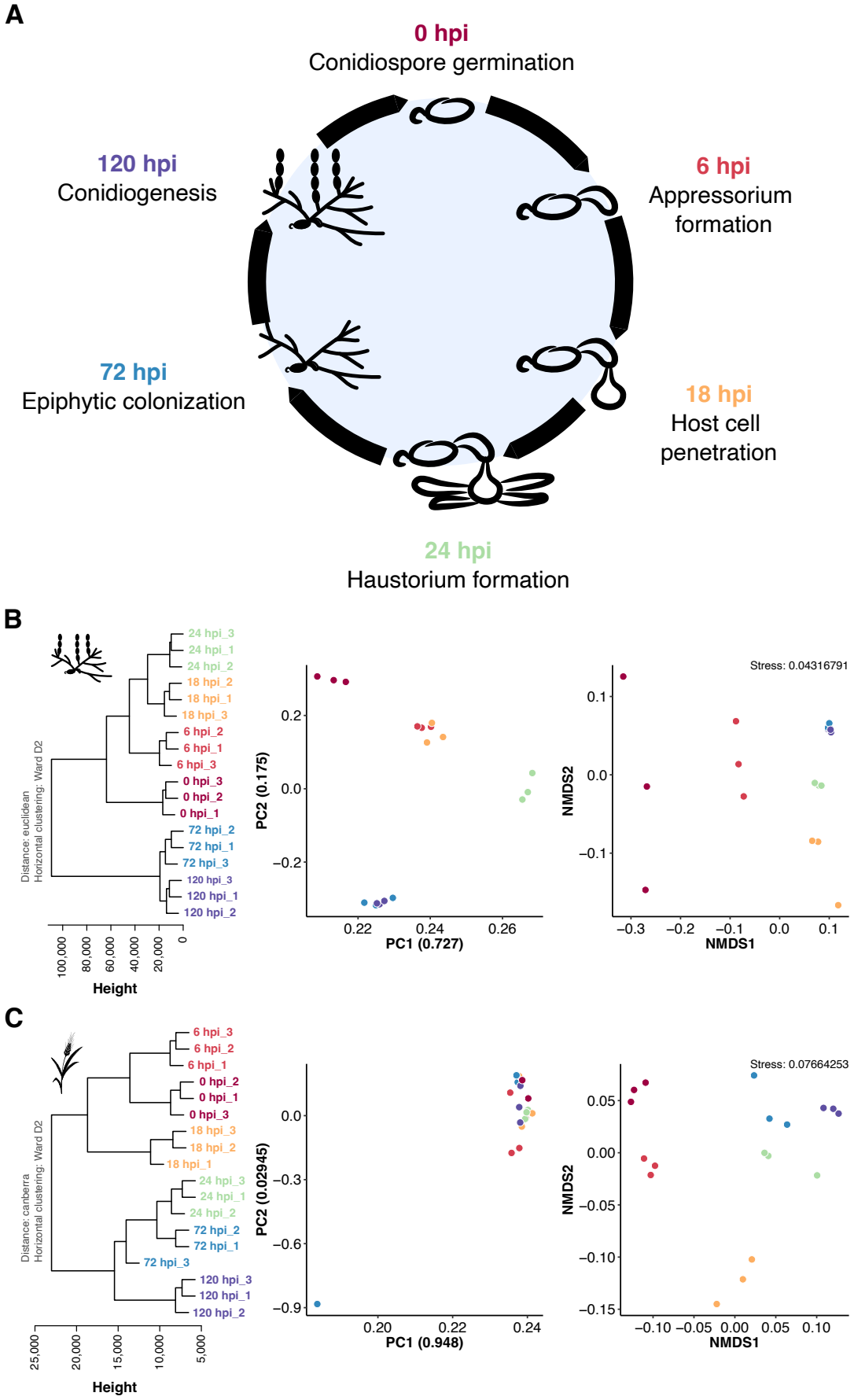
A
0 hpi
Conidiospore germination
6 hpi
Appressorium formation
18 hpi
Host cell penetration
24 hpi
Haustorium formation
72 hpi
Epiphytic colonization
120 hpi
Conidiogenesis
B
24 hpi_3
24 hpi_1
24 hpi_2
18 hpi_2
18 hpi_1
18 hpi_3
6 hpi_2
6 hpi_1
6 hpi_3
0 hpi_3
0 hpi_2
0 hpi_1
72 hpi_2
72 hpi_1
72 hpi_3
120 hpi_3
120 hpi_1
120 hpi_2
Distance: euclidean
Horizontal clustering: Ward D2
Height
PC1 (0.727)
PC2 (0.175)
Stress: 0.04316791
NMDS1
NMDS2
C
6 hpi_3
6 hpi_2
6 hpi_1
0 hpi_2
0 hpi_1
0 hpi_3
18 hpi_3
18 hpi_2
18 hpi_1
24 hpi_3
24 hpi_1
24 hpi_2
72 hpi_2
72 hpi_1
72 hpi_3
120 hpi_3
120 hpi_1
120 hpi_2
Distance: canberra
Horizontal clustering: Ward D2
Height
PC1 (0.948)
PC2 (0.02945)
Stress: 0.07664253
NMDS1
NMDS2

181

182 **Figure 1. RNA-seq data obtained from *B. hordei*-infected barley leaf epidermal peelings**
183 **exhibits time point-dependent clustering.** (**A**) We sampled *B. hord*ei isolate $K1_{AC}$-infected
184 barley abaxial leaf epidermis at time points across the asexual life cycle of the fungus. The
185 pictograms indicate the fungal stage from conidiospore germination (0 hpi) to conidiogenesis, i.e.,
186 asexual spore formation (120 hpi). (**B**) and (**C**) Left panels: Horizontal clustering using the
187 normalized gene expression values of *B. hordei* isolate $K1_{AC}$ (**B**) and *H. vulgare* cv. 'Margret' (**C**),
188 respectively, was calculated with Euclidean distance and Ward.D2 clustering in R. Height
189 indicates the Euclidean distance between samples. Middle panels: Principal components were
190 computed using the R algorithm prcomp. The percentage of sample divergence explained by the
191 principal components PC1 and PC2 are indicated as ratios in the axis labels. Right panels: Non-
192 metric multidimensional scaling (NMDS). Colors: Burgundy, 0 hpi; red, 6 hpi; yellow, 18 hpi; light
193 green, 24 hpi; blue, 72 hpi; purple, 120 hpi.
194
195
196 **TEs are transcriptionally active in a time point-dependent manner in *B. hordei***
197 Since the genome of *B. hordei* is largely occupied by TEs (Spanu et al. 2010; Frantzeskakis
198 et al. 2018), we generated a manually curated (Goubert et al. 2022) database of non-
199 redundant TEs for *B. hordei*. In total, we established 353 consensus repeats including a TE
200 consensus database of 344 TE families, of which 116 were LTR-*Ty3* (aka LTR-*Gypsy*), 122
201 were LTR-*Copia*, 80 were LINE-*Tad1* elements, 3 were unknown LTR-type TEs, 3 were
202 NonLTR retroposons, 2 were SINE (*Eg-R1* and *Egh24*), and 18 were DNA transposons
203 (**Table 1**). We then updated the TE annotation of the *B. hordei* genome with a custom
204 pipeline (**Supplementary Figure 1**). We found that 47,581,730 bp (38.22%) of the *B. hordei*
205 isolate DH14 genome assembly were occupied by LTR retrotransposons, 29,472,397 bp
206 (23.67%) by LINE retrotransposons, 10,208,381 bp (8.20%) by DNA transposons, 4,028,256
207 bp (3.24%) by SINE retrotransposons, and 2,013,553 bp (1.62%) by other or unclassified
208 elements (**Supplementary Table 2**). Overall, we discovered 13,907 full-length (9.4%) and
209 133,617 truncated TEs in the *B. hordei* genome; similarly low full-length conservation was
210 observed in the fungus *Laccaria bicolor* with 6.3% (Labbé et al. 2012). In total, according to
211 the updated calculation, the *B. hordei* reference genome contained 93,304,317 bp (74.95%)
212 interspersed repetitive sequence, which is close to previous estimates (Spanu et al. 2010;
213 Frantzeskakis et al. 2018).
214 Next, we analyzed the expression levels of fungal consensus TEs in the course of
215 pathogenesis. On average, both DNA and LINE and LTR retrotransposons exhibited high
216 (>500 TPM) expression levels (**Figure 2A-B**). Further, using time-resolved analysis of RNA-
217 seq data via TCseq (Wu and Gu 2022) and quantitative reverse transcriptase polymerase
218 chain reaction (qRT-PCR) analysis for selected elements, we found that transposon families

219 can exhibit time point-specific enhanced transcript levels (**Figure 2C-D** and **Supplementary**
220 **Figure 2**), suggestive of dynamic regulation of TE expression in the course of plant infection.
221 Non-coding RNAs are a common means to reversibly silence gene expression (Nicolás and
222 Ruiz-Vázquez 2013; Bologna and Voinnet 2014). Previously, we found that sRNAs often
223 originate from TEs (Kusch et al. 2018) and that phasiRNAs preferentially align to TEs,
224 indicative of RNAi activity on transcripts originating from TEs (Kusch, Singh, et al. 2023). We
225 therefore used publicly available sRNA-seq datasets for *B. hordei* (Hunt et al. 2019; Kusch,
226 Singh, et al. 2023) to assess phasing of consensus TEs via the tool unitas (Gebert et al.
227 2017). Overall, we detected the accumulation of phasiRNA mapping in 104 of the 344
228 consensus TEs (**Table 1**), of which 91 were LTR elements (51 *Ty3* and 40 *Copia* elements)
229 and 13 were *Tad1* LINE elements (**Figure 3A**). These 104 elements corresponded to 1,333
230 full-length and 39,499 truncated TEs in the genome of *B. hordei*. Of these, 102 exhibited
231 expression levels of more than 250 TPM at a minimum of one time point. We compared
232 these apparently phased TEs with TEs showing time point-specific expression patterns
233 (**Figure 2C**) and found 22 to be both phased and undergoing dynamic expression (12 *Ty3*, 7
234 *Copia*, and 3 *Tad1* elements; **Figure 3**). Thus, phasing of TE transcripts may contribute to
235 the dynamic regulation of TEs throughout the pathogenic fungal life cycle.
236 Further, we observed cases of RNA-seq read-mapping to TE loci that exhibited signs of
237 splicing, with splice sites located on the antisense strand of the TE-encoded genes
238 (**Figure 3D**). These transcripts did not appear to encode any meaningful peptides and thus
239 were TE-derived antisense long noncoding RNAs (lncRNAs). We selected eight TE
240 antisense lncRNAs that exhibited expression above 10 TPM at a minimum of one time point,
241 which we successfully amplified, cloned and sequenced (Sanger technology). In two of these
242 (*BLGHnc_000866-RA* and *BLGHnc_004496-RA*), we verified the occurrence of the predicted
243 introns (**Figure 3E** and **Figure 3F**). Collectively, this approach independently validated the
244 existence of, in part intron-containing, TE antisense lncRNAs in *B. hordei*.
245

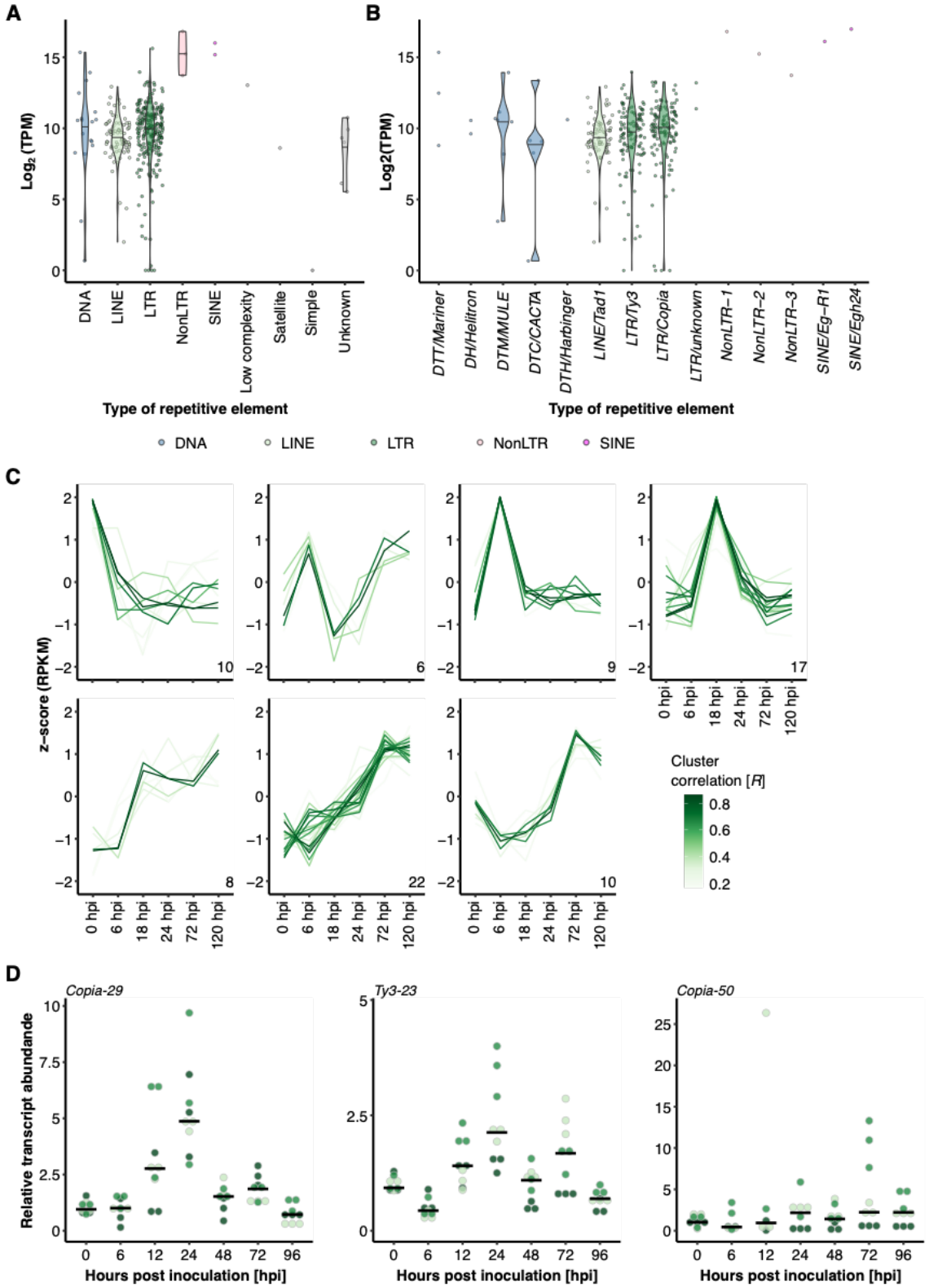

Figure 2. TE families exhibit infection stage-specific expression patterns. (**A**) and (**B**) We mapped the reads from the time-course RNA-seq experiment to our repetitive elements database containing 344 individual non-redundant TE families (**Table 1**). The violin plots show the Log_2 of the average normalized expression (y-axis) of each family expressed as transcripts per million (TPM); the types of repetitive elements (blue, DNA transposons; light green, LINE; dark green,

252 LTR; red, NonLTR retrotransposons; magenta, SINE; grey, low complexity regions, satellites,
253 simple repeats, and unknown repeats) are indicated on the x-axis. (**C**) We used TCseq (Wu and
254 Gu 2022) to cluster time-course expression patterns of the 344 consensus TEs. The lines
255 represent single consensus TEs; the color shade denotes the cluster membership by Spearman
256 correlation (the darker the shade of green, the higher the correlation *R* with the respective
257 expression cluster according to the color scheme). The x-axis denotes the time points of infection
258 (**Figure 1A**), i.e., 0 hpi (conidiospore germination), 6 hpi (appressorium formation), 18 hpi (host
259 cell penetration), 24 hpi (haustorium formation), 72 hpi (epiphytic colonization), and 120 hpi
260 (conidiogenesis). The y-axis indicates the relative z-score based on reads per kb of transcript per
261 million mapped reads (RPKM). (**D**) We conducted qRT-PCR analysis of selected TE families (for
262 the whole set of tested TE families, see **Supplementary Figure 2**). The dot plots display the
263 relative transcript abundance (according to $\Delta\Delta^{CT}$ analysis; y-axis) of the respective TE family
264 indicated on the top-left in *B. hordei* isolate $K1_{AC}$ at seven time points of host infection (x-axis; see
265 also **Figure 1A**). TE transcript levels were normalized to *B. hordei GAPDH* (*BLGH_00691*); three
266 independent replicates ($n = 3$) consisting of three technical replicates each were performed. The
267 shades of green indicate the replicate each data point belongs to; the black bar shows the
268 median.
269
270
271 **Table 1.** Summary of *B. hordei* (isolate DH14) non-redundant consensus repeats.

Type	Family	Number of consensus elements	Median length [bp]	Number of elements in the *B. hordei* reference genome	
				Full-length	Partial
Retrotransposon	LTR/*Ty3*[a]	116	5,686	1,709	27,763
	LTR/*Copia*	122	5,175	1,830	32,351
	LTR/unknown	3	1,599	43	2,571
	LINE/*Tad1*	80	6,057.5	1,303	41,914
	NonLTR/retroposon	3	859	823	2,510
	SINE/*Egh24*	1	884	2,129	5,005
	SINE/*Eg-R1*	1	657	1,667	625
DNA transposon	DTT/*Mariner*	3	1,728	1,295	8,322
	DH/*Helitron*	2	3,506	32	1,002
	DTM/*MULE*	7	4,996	1,336	6,853
	DTC/*CACTA*	5	1,847	1,682	4,567
	DTH/*Harbinger*	1	491	58	134
Other	Satellite	1	15,649	0	158
	Low complexity	1	2,134	7	752
	Simple repeat	1	633	0	14
	Unknown	6	2,468	26	1,709

272 [a] formerly known as *Gypsy*
273
274

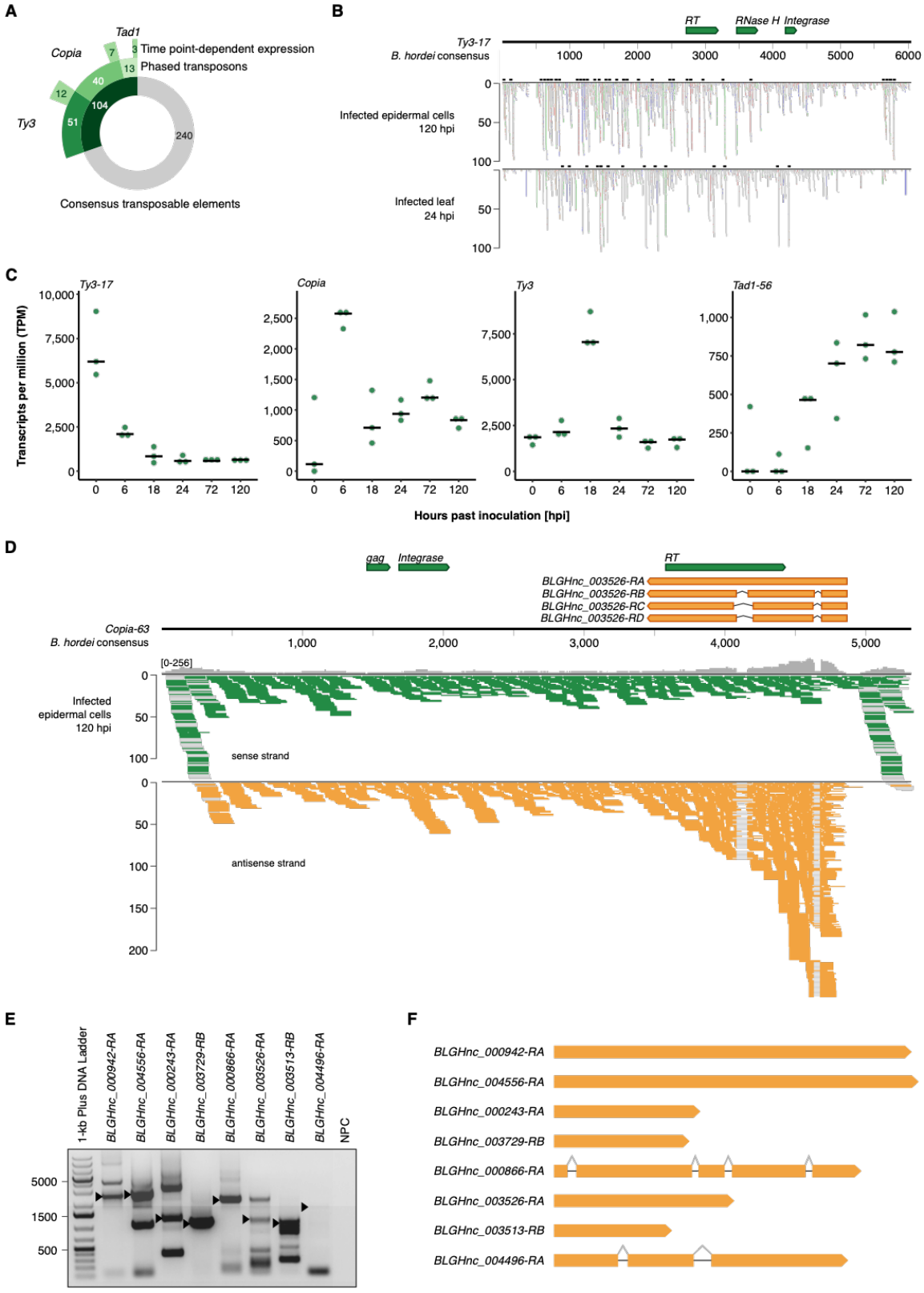

Figure 3. Noncoding RNAs are associated with TEs in *B. hordei*. (**A**) We mapped publicly available sRNA-seq datasets obtained from *B. hordei*-infected barley plants to the TE consensus database using bowtie (Langmead and Salzberg 2012) and identified candidate phasiRNAs using unitas (Gebert et al. 2017). The donut chart shows the number of consensus TEs to which

280 phasiRNAs were linked (green portion of inner circle), the number of elements accounting for the
281 different TE families (**Table 1**; second circle), and the number of consensus TEs whose
282 expression peaks at specific time points (**Figure 2**; outer circle). (**B**) Example of stacked
283 phasiRNAs mapped to the consensus sequence of TE *Ty3-17* (6,054 bp in length). The TE self-
284 propagation genes are indicated on top (green arrows); these genes encode RT (reverse
285 transcriptase), RNase H, and DNA integrase. The scale below the black horizontal line indicates
286 the TE length and position in bp. Mapped sRNAs are shown in the windows below the size scale
287 for two examples: derived from infected leaf epidermal cells at 120 hpi (Kusch, Singh, et al. 2023)
288 and derived from infected total leaf material at 24 hpi (Hunt et al. 2019). Grey blocks indicate
289 single reads; the black boxes on top of each graph display predicted clusters of phasiRNAs.
290 Colored blocks indicate read mismatches with the reference sequence: blue, C; red, T; orange,
291 G; green, A. Data were visualized using Integrative Genomics Viewer v2.9.4 (Robinson et al.
292 2011). (**C**) The dot plot shows the time course expression patterns of selected consensus TEs
293 using the RNA-seq dataset generated in this study. The y-axis shows the normalized expression
294 expressed as transcripts per million (TPM); the x-axis indicates the respective time point of the
295 asexual life cycle of *B. hordei* (**Figure 1A**). The selected TE consensus elements are indicated on
296 the top-left of each plot. (**D**) Example of an antisense lncRNA occurring in the consensus TE
297 *Copia-63* (5,317 bp in length). The upper lane indicates annotated transcripts on the TE, where
298 TE self-propagation genes are indicated in green (genes encode RT (reverse transcriptase), gag
299 polyprotein, and DNA integrase) and three detected isoforms of associated lncRNAs in orange.
300 The scale below the black horizontal line indicates the TE length and position in bp. The two
301 lower panels show RNA-seq read mappings to this TE as colored lines. Green, stranded reads
302 aligning to the sense strand; Orange, stranded reads aligning to the antisense strand. Grey lines
303 indicate reads split due to predicted splicing events. Data were visualized using Integrative
304 Genomics Viewer v2.9.4 (Robinson et al. 2011). (**E**) We amplified several TE antisense lncRNAs
305 from *B. hordei* cDNA using sequence-specific primer pairs. The agarose gel shows PCR-
306 amplified lncRNAs (indicated above each lane), arrows indicate the expected PCR products.
307 Expected PCR amplicon sizes were: *BLGHnc_000942-RA* (*Ty3-23* antisense), 2,831 bp;
308 *BLGHnc_004556-RA* (*Copia-23* antisense), 2,888 bp; *BLGHnc_000243-RA* (*Ty3-1* antisense),
309 1,150 bp; *BLGHnc_003729-RB* (*Ty3-9* antisense), 1,065 bp; *BLGHnc_000866-RA* (*Ty3-62*
310 antisense), 2,187 bp; *BLGHnc_03526-RA* (*Copia-63* antisense), 1,419 bp; *BLGHnc_003513-RB*
311 (intergenic), 922 bp; *BLGHnc_004496-RA* (intergenic), 2,128 bp. Bands corresponding to the
312 expected product size were excised from the gel and their sequence identity confirmed by
313 amplicon sequencing. NPC, no primer control. DNA Ladder, 1 kb plus (Invitrogen-Thermo Fisher,
314 Waltham, MA, USA). (**F**) The genomic transcript models of *BLGHnc_000942-RA*,
315 *BLGHnc_004556-RA*, *BLGHnc_000243-RA*, *BLGHnc_003729-RB*, *BLGHnc_000866-RA*,
316 *BLGHnc_03526-RA*, *BLGHnc_003513-RB*, and *BLGHnc_004496-RA*. Orange blocks represent
317 exons and grey lines spliced introns.

318
319
320 **Genome-wide lncRNA annotation in *B. hordei***
321 We next identified and manually annotated all putative lncRNAs in the genome of *B. hordei*
322 using our extensive time-course RNA-seq dataset. We assembled 45,797 transcripts using
323 StringTie (Pertea et al. 2015) and designed a pipeline to identify lncRNAs (>200 bp and no
324 apparent coding potential) from the assembled transcripts (**Figure 4A**). We used a Web
325 Apollo instance (Lee et al. 2013) to manually inspect and correct coding and noncoding gene
326 models, resulting in 5,127 lncRNA loci across the *B. hordei* genome, accounting for 8,970
327 transcripts in total. Due to the extensive transcriptome data in our study, which was not
328 available for coding gene annotation before (Frantzeskakis et al. 2018), we further detected
329 43 new coding genes in the genome of *B. hordei*, removed 12 models that were located
330 within TEs and encoded predicted transposon replication genes, and corrected another 142
331 models, which changed the coding gene number from 7,118 to 7,149. The most common
332 functional assignments of the 43 newly annotated encoded proteins are predicted candidate
333 secreted effectors, additional Sgk2 kinase-like paralogs, and fungal zinc finger DNA binding
334 domains (**Supplementary Table 3**).
335 We found that lncRNAs were shorter than coding mRNAs on average (1,494.8 bp and
336 2,110.8 bp, respectively) and contained fewer exons (2.3 and 3.0 exons on average;
337 **Figure 4**). More than 50% of lncRNAs consisted of two exons, while lncRNAs with more than
338 five exons were rare (<1.9%). Overall, mRNAs exhibited 15.5-fold higher median expression
339 levels than lncRNAs in our dataset, and there was no significant difference in this respect
340 between intergenic and antisense lncRNAs. In total, 914 intergenic lncRNAs derived from
341 TEs, of which 823 originated from the antisense strand of the respective TE.
342 Furthermore, we found that 2,378 of the 5,127 lncRNA genes encoded more than one
343 transcript variant, suggesting alternative splicing of a substantial portion of the lncRNAs in
344 *B. hordei* (**Figure 4F**). Two lncRNAs gave rise to eleven separate isoforms, another three
345 lncRNAs contained up to nine isoforms, while most lncRNA genes had two (1,488; 62%) or
346 three (555; 23%) transcript variants (**Figure 4F**). The most common alternative splicing event
347 was a retained intron (2,016 events), followed by an alternative 3' splice site (1,163 events;
348 **Figure 4G**). We detected some cases in which alternative lncRNA isoforms showed
349 differential accumulation at different time points during fungal pathogenesis (**Figure 4H**),
350 suggesting that alternative splicing of lncRNAs occurs in a developmental stage-specific
351 manner in *B. hordei*.
352
353

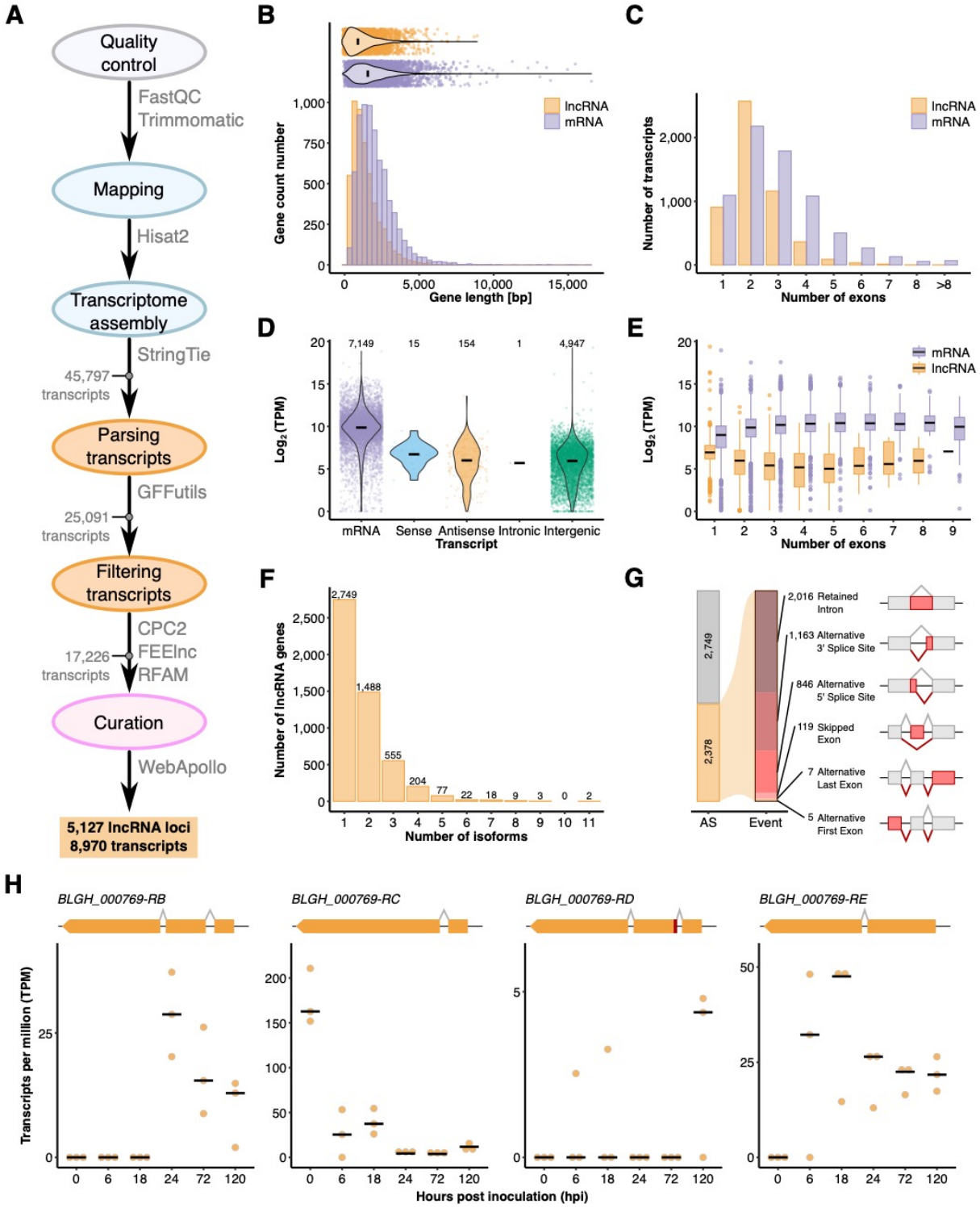

Figure 4. Genome-wide identification and characterization of *B. hordei* lncRNAs. (**A**) Using the total RNA-seq data mapped to the genome of *B. hordei* isolate DH14 (Frantzeskakis et al. 2018) with HISAT2 (Kim et al. 2015), we assembled transcripts with StringTie (Pertea et al. 2015). Next, we filtered out coding genes from the transcriptome by Gffcompare (Pertea and Pertea 2020), transcripts shorter than 200 bp using Gffread (Pertea and Pertea 2020), transcripts with coding potential using CPC2 (Kang et al. 2017), and transcripts accounting for ribosomal RNA, transfer RNA, small nuclear RNA, and small nucleolar RNA via CMscan search against the

362 Rfam database (Kalvari et al. 2018). Then, we used FEELnc (Wucher et al. 2017) for lncRNA
363 annotation and classification, resulting in 17,226 putative lncRNAs in the reference genome of
364 *B. hordei*. Lastly, we manually inspected the predicted lncRNA models by our Web Apollo (Lee et
365 al. 2013) instance, yielding in total 5,127 unique lncRNA loci in *B. hordei*. (**B**) Histogram for the
366 transcript length in base pairs (bp; x-axis) against the number of coding genes (mRNAs, purple)
367 and lncRNAs (orange; y-axis). The violin plot above shows the overall distribution of gene
368 lengths; data points represent individual transcripts. (**C**) Bar graph of the exon number per
369 transcript (x-axis) against the gene number (y-axis). Purple, mRNAs; orange, lncRNAs. (**D**) The
370 violin plot shows the expression in Log_2(transcripts per million (TPM)) for mRNAs (purple),
371 lncRNAs in sense orientation of associated genes (blue), lncRNAs in antisense orientation of TEs
372 (orange), intronic lncRNAs (grey), and intergenic lncRNAs (green). The number of transcripts (*n*)
373 contributing to the respective subset are given on the top. (**E**) The box plot shows the transcript
374 levels in Log_2(TPM) for lncRNAs (orange) and mRNAs (purple) depending on the transcript exon
375 number (x-axis). (**F**) The histogram shows the number of transcripts (x-axis) encoded by lncRNA
376 genes (y-axis). (**G**) The stacked bar graph displays the occurrence of alternatively spliced lncRNA
377 transcripts (AS, alternative splicing; orange bar) and the number and type of alternative splicing
378 events in *B. hordei*. The types of events are illustrated by the drawings, where the red portion of
379 the exon indicates the alternative event and black lines connecting exons splice events, colored
380 in shades of red and orange according to event. From dark red to dark orange, events are shown
381 in this order: retained intron, alternative 3' splice site, alternative 5' splice site, skipped exon,
382 alternative last exon, and alternative first exon. (**H**) The dot plots show the transcript levels in
383 transcripts per million (TPM) for alternatively spliced isoforms of the lncRNA *BLGHnc_000769* (y-
384 axis) at six time points of host infection (x-axis). Note that isoform *BLGHnc_000769-RA* was not
385 expressed above background levels and thus omitted from this Figure. The black bar indicates
386 the median of three independent replicates (*n*=3).
387
388
389 **Gene expression patterns in *B. hordei* reflect its pathogenic development**
390 Transcripts are differentially regulated in *B. hordei* during its pathogenic development
391 (**Figure 1B and C**). To gain detailed insights into (co-)expression profiles, we assigned all
392 reads mapping to the *B. hordei* reference genome to the annotated 7,149 coding genes and
393 5,127 lncRNAs (**Supplementary Table 4** for TPM values). We then clustered lncRNA and
394 mRNA gene expression patterns across all time points using TCseq (Wu and Gu 2022) and
395 identified nine distinct co-expression clusters featuring 2,264 lncRNAs and 2,762 coding
396 genes in total (**Figure 5A**). The clusters exhibited distinct expression patterns, with peaks of
397 transcript accumulation at different time points. Seven clusters showed transcript peaks at
398 one or two specific time points. Cluster 4, comprising transcripts whose levels peaked at
399 18 hpi, contained the highest number of transcripts, namely 336 mRNAs and 344 lncRNAs

400 (**Table 2**). We further analyzed the expression pattern of all genes encoding putative
401 secreted proteins in *B. hordei* and found distinct sets of these genes with peaked transcript
402 levels at 0, 6, 18-24, or 72-120 hpi, indicative of "waves" of genes coding for secreted
403 proteins expressed during fungal pathogenesis (**Figure 5B**). Clusters 4, 5, 6, and 8
404 contained an elevated number of putative secreted proteins (>20% of coding transcripts
405 each), coinciding with peaked transcript accumulation at 18, 24, or 72 hpi (**Figure 5C** and
406 **Table 2**). By contrast, genes encoding Sgk2-like serine/threonine kinases, which are
407 abundant in the genome of *B. hordei* (Kusch et al. 2014), almost exclusively occurred in
408 cluster 9, which represents genes expressed at 120 hpi (**Figure 5C** and **Table 2**).
409 We conducted gene ontology (GO) enrichment analysis for the coding genes found in the
410 nine clusters described above (**Figure 5A**). While no enrichment was detected in case of
411 0 hpi (clusters 1 and 2), we found GO processes related to cell division, cell cycle,
412 microtubule activity processes, oligosaccharide metabolism, response to stimulus, and DNA
413 repair to be enriched at 6 hpi (cluster 3; **Figure 5D**; **Supplementary Table 5**). At 18 and
414 24 hpi, the process "ribonuclease activity" was enriched, likely reflecting an abundance of
415 RNase-like candidate secreted effector proteins (Pedersen et al. 2012; Spanu 2017)
416 expressed at this time point (cluster 5). During late infection (72 hpi and thereafter; clusters 7
417 and 8), processes related to protein, nucleotide, and fatty acid biosynthesis and gene
418 expression were over-represented. Finally, at 120 hpi (cluster 9), processes related to protein
419 phosphorylation and phosphorus metabolism were enriched. Protein phosphorylation was
420 likely enriched due to the high number of Sgk2-like serine/threonine kinases ((Kusch et al.
421 2014); 52 in total; 19.4% of mRNAs in cluster 9; **Table 2**) expressed at 120 hpi (**Figure 5C**
422 and **D**).
423 We conducted the time-course expression and GO enrichment analysis for the plant side as
424 well (**Supplementary Table 6** and **Supplementary Figure 3**). In the host barley, we found
425 eight co-expression clusters, with peaks at 0, 6, 18, 24, or 120 hpi, and a cluster of 646
426 genes exhibiting distinct down-regulation at 6 and 18 hpi (cluster 6; **Supplementary**
427 **Figure 3A**). Processes related to stress or defense response, carbohydrate biosynthesis,
428 and cell wall biogenesis were associated with early-responding genes (6 hpi to 24 hpi;
429 clusters 2-5), but these processes were also over-represented in cluster 6, i.e., the set of 646
430 genes that were down-regulated at 18 hpi. At 72 hpi and 120 hpi, sulfur, nitrogen, organic
431 acid metabolism-related, and catabolism terms were highly represented, in addition to biotic
432 stress response (cluster 7 and 8). Overall, we found that early developmental processes and
433 stress response genes dominated the early infection stage of *B. hordei*, while processes
434 related to growth and metabolic activity were enriched at later stages (**Figure 5A** and **D**).
435 Effector candidates were expressed in at least four waves (**Figure 5B**), while Sgk2-like
436 serine/threonine kinases appeared to be associated mostly with the asexual late infection
437 stages in *B. hordei* (**Figure 5C** and **Table 2**).

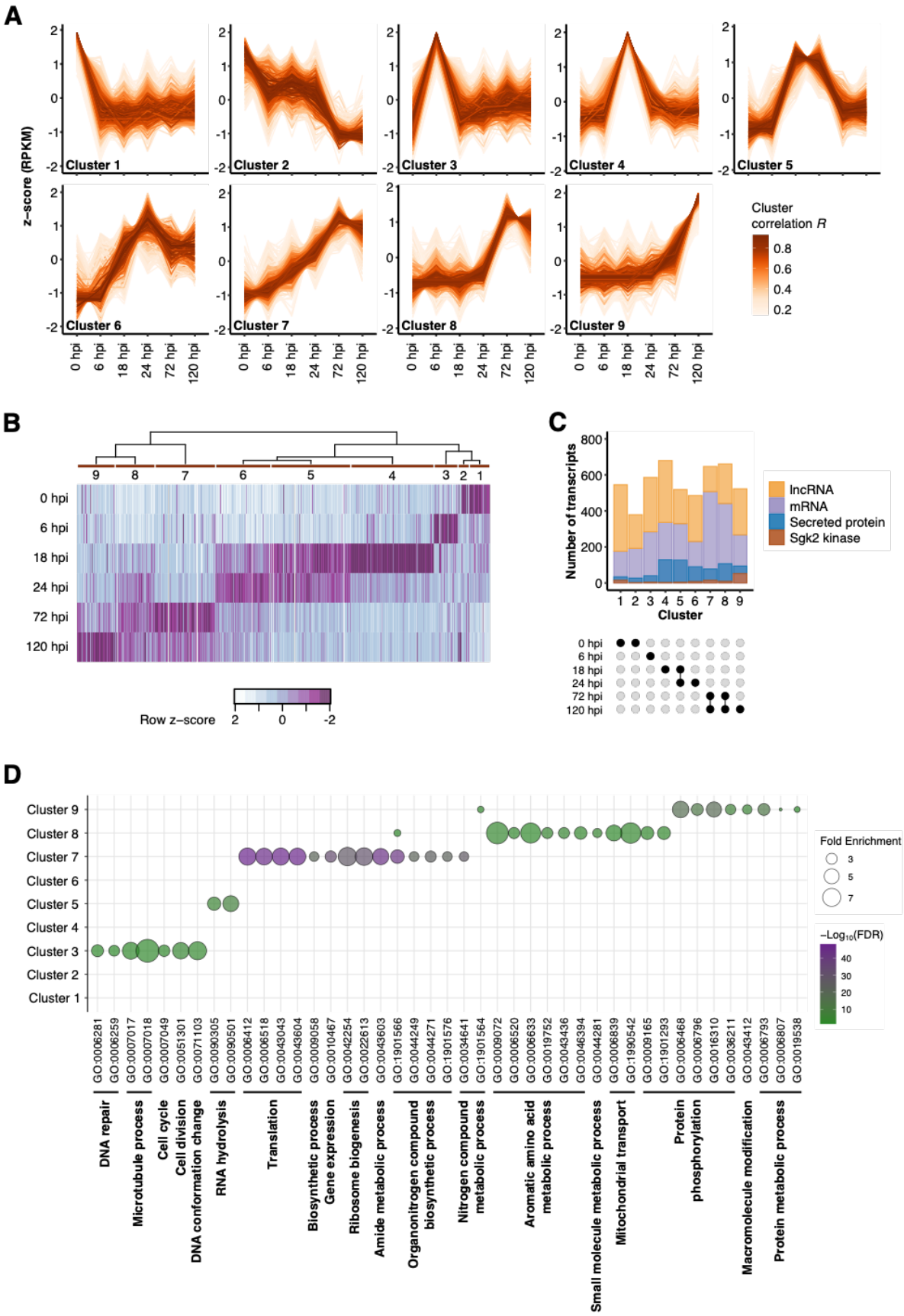

Figure 5. *B. hordei* exhibits infection stage-dependent expression patterns of coding genes and lncRNAs. (**A**) We used TCseq (Wu and Gu 2022) to cluster time-resolved coding

441 gene and lncRNA expression patterns. The lines represent single transcripts; the color shade
442 denotes the cluster membership by Spearman correlation (the darker the shade of orange, the
443 higher the correlation *R* with the respective expression cluster according to the color scheme).
444 The x-axis denotes the time points of infection (**Figure 1A**), i.e., 0 hpi (conidiospore germination),
445 6 hpi (appressorium formation), 18 hpi (host cell penetration), 24 hpi (haustorium formation),
446 72 hpi (epiphytic colonization), and 120 hpi (conidiogenesis). The y-axis indicates the relative z-
447 score based on reads per kb of transcript per million mapped reads (RPKM). (**B**) The heat map
448 shows the relative median expression of genes encoding putative secreted proteins across the
449 time points according to the color scheme below the heat map. Purple indicates high and white
450 low expression. The time course cluster number (**A**) is indicated next to the dendrogram above
451 the heat map. (**C**) The stacked bar graph shows the number of lncRNAs (orange) and mRNAs
452 (purple) in each cluster, indicating mRNAs encoding putative secreted proteins (blue) or Sgk2-like
453 kinases (brown). The x-axis indicates the co-expression cluster (**A**) and is annotated with a dot
454 plot below to highlight the time point represented by each cluster. The y-axis shows the number
455 of transcripts. (**D**) We conducted gene ontology (GO) enrichment analysis for the coding genes
456 from each cluster (A) using ShinyGO v0.77 (Ge et al. 2020) accessed online at
457 http://bioinformatics.sdstate.edu/go/, and summarized GO terms with REVIGO (Supek et al.
458 2011). The dot plot shows the fold enrichment of functional terms compared to the full set of
459 genes of *B. hordei* (dot size); the fill color denotes the $-Log_{10}$(FDR-adjusted enrichment *p* value)
460 according to the color scheme on the right. The summarizing GO descriptions are provided below
461 the GO identifiers (x-axis), the respective co-expression cluster (**A**) is indicated on the y-axis.
462
463
464 **Table 2.** Transcripts in co-expression clusters of *B. hordei*.

			mRNAs encoding			
Cluster	**LncRNAs**	**mRNAs**	Secreted protein	[%]	Sgk2 kinase	[%]
1	369	176	19	10.8%	15	8.5%
2	187	192	25	13.0%	2	0.1%
3	302	284	36	12.7%	4	0.1%
4	344	336	126	37.5%	3	0.1%
5	190	329	123	37.3%	4	0.1%
6	256	230	82	35.6%	8	3.5%
7	140	507	63	12.4%	15	0.3%
8	220	441	98	22.2%	9	0.2%
9	256	267	42	15.7%	52	19.4%

465
466

467 ***B. hordei* lncRNAs may co-regulate transcripts in *cis* and *trans***
468 We noted that lncRNAs, mRNAs, and TEs all exhibited time point-specific expression peaks
469 (**Figure 6A**). Thus, we conducted a weighted gene co-expression network analysis
470 (WGCNA) including all *B. hordei* mRNAs, lncRNAs, and TEs to identify possible co-
471 expression networks and infer putative regulatory networks (**Supplementary Figure 4**). We
472 detected 14 co-expression networks consisting of at least ten transcripts each (**Figure 6B**).
473 Then, we determined the genomic physical distance between the genes encoding these
474 transcripts and calculated the Pearson's correlation coefficient (PCC) *R* value with a cut-off
475 of $|R| \geq 0.7$ (*cis*) or $|R| \geq 0.9$ (*trans*) to discover positive and negative co-regulation of
476 lncRNAs with mRNAs (**Supplementary Table 7**), or a cut-off of $|R| \geq 0.7$ for lncRNA co-
477 regulation with consensus TEs (**Supplementary Table 8**). We regarded *cis* co-regulated
478 lncRNAs and mRNA if their maximal genomic distance was 10 kb, otherwise the respective
479 pair was regarded co-regulated in *trans*. Overall, positive co-regulation was more common
480 than negative co-regulation, and co-regulation was more common in *trans* than in *cis*. In case
481 of lncRNA-mRNA regulons, we detected 6,018 positively and 339 negatively co-regulated
482 *trans* pairs, and 109 positively and 13 negatively co-regulated *cis* pairs. For lncRNA-
483 consensus TE co-regulation, we found 6,169 positive and 334 negative interactions in *trans*.
484 Further, we detected seven negative co-regulation cases of TE antisense lncRNAs and their
485 respective TE, such as *BLGHnc_000540-RA* located antisense of *Copia-23* and
486 *BLGHnc_002596-RA*, an antisense lncRNA of *Ty3-9* (**Figure 6C** and **Figure 6D**).
487 Meanwhile, six TE antisense lncRNAs were positively regulated with the respective TE, such
488 as *BLGHnc_004551-RA* and *Ty3-48* and (**Figure 6E**). Our findings suggest that some
489 transposon antisense lncRNAs may directly regulate the TE they derive from, although the
490 majority of these are co-regulated with distal TEs or mRNAs.
491
492

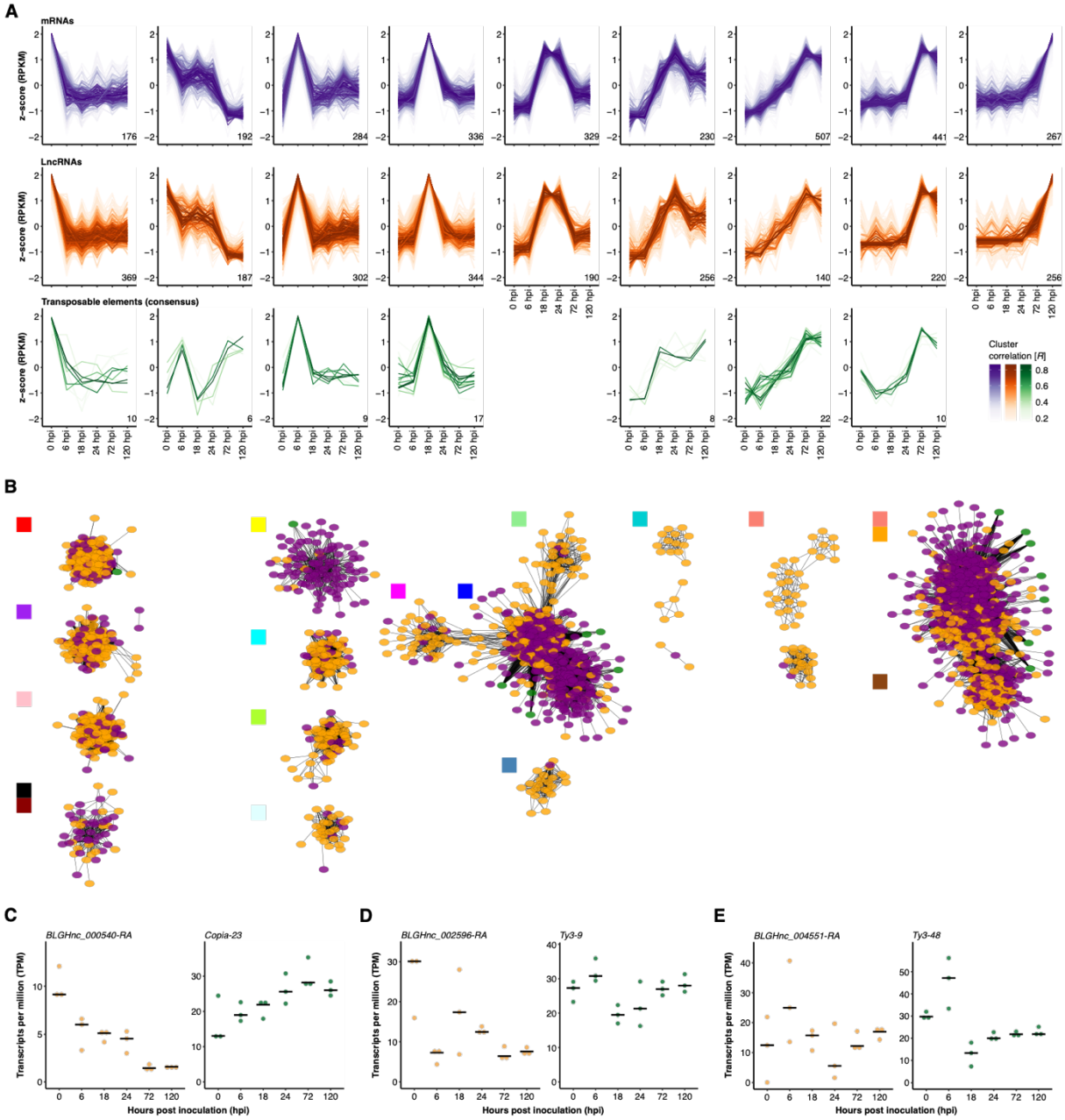

Figure 6. Co-expression patterns of TEs and lncRNAs in *B. hordei*. (**A**) We used TCseq (Wu and Gu 2022) to cluster time-resolved coding gene (mRNA), lncRNA, and consensus TE expression patterns. Each line represents a single transcript; the color shade indicates the cluster membership according to Spearman correlation (the darker the color, the higher the correlation *R* with the respective expression cluster; see color scheme in the bottom right corner). Shades of purple (upper panel), mRNAs; shades of orange (middle panel), lncRNAs; shades of green (bottom panel), consensus TEs. The x-axis indicates the time points of infection: 0 hpi (spore germination), 6 hpi (appressorium formation), 18 hpi (early primary haustorium), 24 hpi (mature primary haustorium), 72 hpi (host colonization), and 120 hpi (conidia formation). The y-axis displays the relative z-score based on reads per kb of transcript per million mapped reads (RPKM). (**B**) Co-regulation networks were discovered using WGCNA (Langfelder and Horvath

2008). The colored circles indicate transcripts (purple, mRNA; orange, lncRNA; green, consensus TE) and lines significant correlation between two transcripts. The WGCNA-assigned cluster colors are indicated on the top-left of each corresponding cluster of transcripts. The clusters were arranged to correspond to the time-resolved expression patterns shown above in (**A**). (**C-E**) The dot plots show examples of expression patterns of TE antisense lncRNA and the corresponding TE, as indicated on top of each plot. Expression values are shown as transcripts per million (TPM; y-axis) during six time points of host infection (x-axis; **Figure 1A**). The black bar indicates the median of three independent replicates (*n*=3).

Discussion

TEs are highly abundant in the genomes of powdery mildew fungi, including *B. hordei* (Spanu et al. 2010; Kusch, Qian, et al. 2023), but their transcript levels have not been measured so far. High-throughput datasets using next-generation sequencing technologies can be powerful tools to understand powdery mildew biology and evolution (Bindschedler et al. 2016). Here, we generated a comprehensive stranded RNA-seq dataset that contains information about all fungal and host transcripts based on random rather than oligo-dT priming during cDNA synthesis. Our dataset covers all major stages of *B. hordei* during the asexual infection cycle on barley, from early conidiospore germination to sporulation (**Figure 1A**). Limitations of the dataset are that (1) the reads are derived from only one isolate (*B. hordei* $K1_{AC}$; (Barsoum et al. 2020)) during the compatible interaction with its host barley, (2) we did not include the sexual reproduction stages, and (3) the short reads preclude precise assignment to individual TE members. However, our data allowed us to provide a genome-wide curated annotation of lncRNAs and their alternatively spliced isoforms (**Figure 4**) and to measure stage-specific transcript accumulation of coding genes, noncoding RNAs, and TEs simultaneously (**Figure 2**, **Figure 5**, **Figure 6**). Altogether, our findings suggest a TE regulatory network involving both (phased) sRNAs (**Figure 3**) and lncRNAs (**Figure 6**). Despite applying a more stringent significance cut-off for *trans*-regulated pairs, our analysis recovered >10-times more *trans*- than *cis*-regulated pairs. Examples of *trans*-co-regulation of lncRNAs with other transcripts in fungi are rare (Till, Pucher, et al. 2018). The per-chance occurrence of co-regulated transcripts increases exponentially when removing spatial constraints; thus, global co-expression networks should be interpreted carefully.

Active TEs can dramatically change the architecture of a genome, including gene disruption or dysregulation, gene duplication, and structural variation (Slotkin and Martienssen 2007; Chuong et al. 2017). While they threaten genome integrity and thus survival, TE-induced

542 variations also increase adaptability under stressful conditions like host immunity. This high
543 risk-high reward relationship has been referred to as a devil's bargain between plant
544 pathogens and TEs (Fouché et al. 2021). Indeed, the cereal powdery mildews *B. hordei* and
545 *B. graminis* f.sp. *tritici* exhibit extensive copy number variation of effector-coding genes,
546 possibly as a consequence of the escape of the recognition of the respective gene products
547 by host resistance proteins (Frantzeskakis et al. 2018; Müller et al. 2019; Saur et al. 2021).
548 Considering the missing RIP mechanism (Spanu et al. 2010; Kusch, Qian, et al. 2023),
549 powdery mildew fungi are likely to possess powerful alternative TE regulating mechanisms to
550 limit the risk of their activity. TEs are often regulated epigenetically or by RNAi (Slotkin and
551 Martienssen 2007), and we previously found signs of sRNA phasing linked to *B. hordei* TEs
552 (Kusch et al. 2018; Kusch, Qian, et al. 2023). Here, we confirmed that phasiRNAs are
553 abundant in 104 of 344 consensus TEs (**Figure 3**), suggesting that RNAi is a major
554 mechanism to regulate TE activity in *B. hordei*.
555 We found TE antisense lncRNAs, in part spliced, in *B. hordei* (**Figure 3**), which showed both
556 positive and negative co-regulation with the TE they derived from (**Figure 6**). TEs can give
557 rise to novel lncRNAs in vertebrates (Kapusta et al. 2013; Cho 2018) and plants (Lv et al.
558 2019; Ariel and Manavella 2021). According to the repeat insertion of domains of lncRNAs
559 (RIDL) hypothesis, TEs can insert into and then become functional domains of lncRNAs, thus
560 driving the emergence, evolution, and functional diversity of lncRNAs (Johnson and Guigó
561 2014; Fort et al. 2021). TEs can also give rise to lncRNAs that contribute to regulatory
562 networks under stressful conditions in plants (Lv et al. 2019; Blein et al. 2020). TE-derived
563 lncRNAs respond differently to phosphate stress between two ecotypes in *Arabidopsis*
564 *thaliana* (Blein et al. 2020), while mutation of the abiotic stress-responsive TE-derived
565 lncRNA *lincRNA11195* impairs the response to abscisic acid and root development in
566 *A. thaliana* (Wang et al. 2017). TE-derived lncRNAs in plants may also regulate gene
567 expression as competing endogenous RNAs acting, for instance, as miRNA sponges, or
568 through interaction with chromatin remodeling complexes (Ariel and Manavella 2021). Fungi
569 are also able to activate TEs in response to biotic or abiotic stress (Choi et al. 2022; Kalem
570 and Panepinto 2022), like the Septoria leaf blotch pathogen *Zymoseptoria tritici* inducing
571 expression of distinct sets of TEs under conditions of starvation or during wheat infection
572 (Fouché et al. 2020). Likewise, the rice bast pathogen *M. oryzae* exhibits lncRNA expression
573 specifically during host infection (Choi et al. 2022), which is comparable to our observations
574 of infection stage-specific induction of lncRNAs in *B. hordei* throughout barley infection. Our
575 data lends support to two scenarios: (1) TE antisense lncRNAs arise due to active TE
576 expression and permit their own down-regulation, for example, by inducing RNAi, and (2)
577 lncRNAs are expressed independently of the activity of the TE they derive from and fulfil
578 distinct regulatory functions.

579 Appropriate transcriptional programs are key for organisms to respond effectively to
580 environmental cues. Transcriptional programs appear to be responsive to cues from the
581 respective host in broad-range plant pathogens (Kusch et al. 2022) and drive lifestyle
582 transitions in hemi-biotrophic plant pathogens, such as *Fusarium* and *Colletotrichum* species
583 (O'Connell et al. 2012; Hill et al. 2022). Likewise, obligate biotrophic and host-specialized
584 pathogens, such as *B. hordei*, are likely responsive to various host-derived signals to activate
585 suitable transcriptional programs throughout its pathogenic life cycle. Similar to previous
586 findings in *B. hordei* infecting the hypersusceptible non-host mutant plant *Arabidopsis*
587 *thaliana pen2 pad4 sag101* (Hacquard et al. 2013), we observed distinct sets of effector
588 candidate-encoding genes to be transcriptionally induced at specific stages of barley
589 infection (**Figure 5B**). A previous microarray study also found one class of effectors to be
590 transcribed at pre-penetration but not post-penetration stages in *B. hordei* (Both, Eckert, et
591 al. 2005). The different pathogenic stages are likely to require different sets of effectors
592 conducting functions appropriate for the respective phase of infection (Stergiopoulos and De
593 Wit 2009; Lo Presti et al. 2015). For instance, early infection stages prior to successful host
594 cell penetration probably require the aggressive suppression of host immunity, while
595 subsequent steps also depend on reprogramming of the host plants' secretory system
596 (Schmidt et al. 2014; Liao et al. 2023), metabolism, and source-sink status (Djamei et al.
597 2011; Cai et al. 2023). Likewise, we observed that stress response genes are induced in
598 *B. hordei* during early infection, when the fungus faces the strongest resistance in the form of
599 the generation of reactive oxygen species and the biosynthesis and delivery of antimicrobial
600 compounds (**Figure 5D**). Indeed, barley showed up-regulation of defense response and cell
601 wall biogenesis-related genes, but also down-regulation of such genes at 18 hpi. Contrary to
602 previous microarray studies (Both, Csukai, et al. 2005; Both, Eckert, et al. 2005), we also
603 observed cell cycle, cell division, and microtubule processes at the early infection stage.
604 However, these processes may have been missed in the previous analysis as genome
605 information was lacking and, in contrast to microarrays, which are limited to known probes,
606 RNA-seq recovers all expressed genes in an organism. Meanwhile, genes encoding proteins
607 functioning in sulfur, nitrogen, and organic molecule biosynthesis showed elevated transcript
608 levels at 72 hpi, after successful colonization of the plant by *B. hordei* (**Supplementary**
609 **Figure 3**). In line with previous observations (Both, Csukai, et al. 2005; Both, Eckert, et al.
610 2005), protein and nucleic acid metabolic processes and protein biosynthesis including
611 translation and ribosome biogenesis were enriched after 72 hpi. At late infection stages,
612 processes related to vegetative growth, gene expression, and metabolism dominated in
613 *B. hordei*, suggestive of an undermined plant immune system and a supply of metabolites to
614 fuel biosynthetic processes.
615 It has not escaped our attention that TE-derived lncRNAs might give rise to novel coding
616 genes in the course of evolution. These genes could encode novel effectors that help

617 establish and maintain the biotrophic interaction with the host plant. In a similar case, the
618 *B. hordei* effector ROP-interactive peptide 1 (ROPIP1) originates from a *SINE/Eg-R1* TE and
619 transmits to barley host cells in the course of infection, where it interacts with barley RACB
620 and disrupts cortical microtubules (Nottensteiner et al. 2018). Thus, ROPIP1 promotes the
621 infection success of *B. hordei* on barley. The large number of TE antisense lncRNAs in
622 *B. hordei* implies that *B. hordei* and possibly fungal plant pathogens with TE-enriched
623 genomes in general repurpose TEs for the invention of novel genes to encode effector
624 proteins.
625
626

627 Materials and methods

628

629 **Plant and pathogen cultivation**

630 Plants of barley (*H. vulgare* cv. 'Margret') were cultivated in SoMi513 soil (Hawita, Vechta,
631 Germany) in a long-day cycle (16 h light period at 23 °C, 8 h dark at 20 °C) at 60-65%
632 relative humidity and a light intensity of 105-120 µmol s^{-1} m^{-2}. Plants were inoculated with
633 *B. hordei* strain $K1_{AC}$ at seven days after germination and then transferred to isolated growth
634 chambers with a long day cycle (12 h light at 20 °C, 12 h dark at 19 °C), approximately 60%
635 relative humidity, and 100 µmol s^{-1} m^{-2} light intensity.
636

637 **RNA sampling and RNA sequencing**

638 We collected B. *hordei*-infected barley abaxial leaf epidermis at 0, 6, 18, 24, 72, and 120 hpi
639 using an epidermal peeling method (Li et al. 2019) to enrich for fungal RNAs and infected
640 epidermal cells. The epidermal peels were ground to a fine powder in liquid nitrogen using
641 mortar and pestle and RNA isolated via TRIzol (Thermo Scientific, Karlsruhe, Germany)
642 according to the manufacturer's instructions. Genomic DNA was removed using DNase I
643 (RNase-free, Thermo Scientific). RNA integrity was determined by microcapillary
644 electrophoresis (2100 BioAnalyzier system; Agilent, Santa Clara, CA, USA) and RNA
645 quantity by spectrophotometry (NanoDrop; Thermo Scientific) and spectrofluorimetry (Qubit;
646 Thermo Scientific). We sent 18 high-quality total RNA samples (RIN > 6.0, c[RNA] >
647 100 ng μL^{-1}, m[RNA] > 2 μg) for stranded RNA sequencing at 150-bp paired-end reads,
648 random oligomer priming to recover total RNA, and plant/animal ribosomal RNA depletion,
649 provided by Novogene Europe, Cambridge Science Park, UK. The raw data was inspected
650 using FastQC v0.11.5 (Babraham Bioinformatics, UK) and overrepresented sequences
651 identified by nucleotide BLAST in April 2021 (https://blast.ncbi.nlm.nih.gov/Blast.cgi). Reads
652 were adapter- and quality-trimmed with Trimmomatic v0.36 (Bolger et al. 2014) before further
653 usage.

654

655 **Quantitative reverse transcriptase PCR (qRT-PCR)**

656 We collected barley leaf epidermal peelings (see above) at 0, 6, 12, 24, 48, 72, and 96 hpi in
657 three biological replicates. RNA isolation and quality control were done as described above.
658 Complementary DNA (cDNA) was synthesized using the High-Capacity RNA-to-cDNA Kit
659 (Applied Biosystems-Thermo Fisher, Schwerte, Germany) and stored at -20 °C. The cDNA
660 was diluted 1:10 prior to further experiments. We conducted qRT-PCRs with the Takyon No
661 ROX SYBR MasterMix blue dTTP Kit (Eurogentec, Seraing, Belgium) in a LightCycler 480 II
662 (Roche, Basel, Switzerland). The PCR efficiency of all primers used in this study
663 (**Supplementary Table 9**) was between 1.8 and 2.0 and the annealing temperature was set
664 to 58 °C. Melting curve analysis validated in each case the synthesis of single amplicons.
665 Expression levels of target TEs was evaluated relative to the housekeeping gene *GAPDH*
666 (*BLGH_00691*) of *B. hordei* (Pennington et al. 2015). We calculated relative transcript
667 abundance with $2^{-(CT(target) - CT(GAPDH))}$ according to the $\Delta\Delta^{CT}$ method (Livak and Schmittgen
668 2001).

669

670 **Annotation of TEs**

671 We used a TE annotation pipeline integrating homology-based and *de novo* structural based
672 methods. We used the EDTA pipeline (Ou et al. 2019) to annotate TE elements with the help
673 of the *Blumeria* TE consensus sequences from RepBase v20181026. Then, CD-HIT-EST (Fu
674 et al. 2012) was used to merge similar sequences in the *B. hordei* isolate DH14 reference
675 genome assembly (Frantzeskakis et al. 2018). Next, we created an updated TE consensus
676 database by multiple sequence alignment and manual curation of consensus TEs (Goubert
677 et al. 2022), which we then used for genome-wide re-annotation of TEs with RepeatMasker
678 (Smit et al. 2016) using the TE consensus library as database.

679

680 **Detection and annotation of lncRNAs**

681 First, we mapped the trimmed total RNA-seq read data to the *B. hordei* isolate DH14 genome
682 (Frantzeskakis et al. 2018) using HISAT2 (Kim et al. 2015). We extracted mapping reads for
683 transcriptome assembly with StringTie (Pertea et al. 2015) and then filtered out coding genes
684 from the transcriptome via Gffcompare (Pertea and Pertea 2020), transcripts shorter than
685 200 bp using Gffread (Pertea and Pertea 2020), transcripts with coding potential using CPC2
686 (Kang et al. 2017), and transcripts accounting for ribosomal RNA, transfer RNA, small
687 nuclear RNA, and small nucleolar RNA via CMscan search against the Rfam database
688 (Kalvari et al. 2018). Then, we performed lncRNA annotation and classification with FEELnc
689 (Wucher et al. 2017), predicting 17,226 putative lncRNAs in the *B. hordei* genome. We used
690 a WebApollo instance (Lee et al. 2013) to manually inspect the predicted lncRNA models,
691 and to annotate all possible transcript isoforms for each lncRNA gene.

692
693 **Functional annotation of newly discovered gene models in *B. hordei***
694 Peptide sequences deriving from gene models newly discovered in the genome of *B. hordei*
695 DH14 (Frantzeskakis et al. 2018) during annotation of lncRNAs were functionally analyzed
696 for signal peptides using SignalP5.0 (Almagro Armenteros et al. 2019), transmembrane
697 domains via TMHMM v2 (Krogh et al. 2001), sequence homology using BLASTP
698 (https://blast.ncbi.nlm.nih.gov accessed May 2023), and functional domains using
699 InterProScan v5.62-94.0 (Jones et al. 2014) and hmmscan via the HMMER web server
700 v2.41.2. accessed May 2023 (Eddy 2011; Potter et al. 2018).
701
702 **Cloning of lncRNA candidates**
703 We amplified lncRNAs from isolated RNA or cDNA from samples used for RNA-seq or qRT-
704 PCR and lncRNA-specific primer pairs (**Supplementary Table 7**). The PCR products were
705 purified using Phusion High-Fidelity DNA polymerase (New England Biolabs, Frankfurt a.M.,
706 Germany) and subsequently ligated into the vector system pCR-Blunt II-TOPO via the Zero
707 Blunt™ TOPO™ PCR cloning kit (Thermo Fisher Scientific). The lncRNA sequences were
708 confirmed by Sanger chain-termination sequencing provided by eurofins Genomics
709 (Ebersberg, Germany).
710
711 **Time-course transcript expression analysis with RNA-seq data**
712 We mapped the trimmed total RNA-seq data to the genomes of *B. hordei* isolate DH14
713 (Frantzeskakis et al. 2018) or *H. vulgare* cv. 'Morex' (Mascher et al. 2021) using HISAT2
714 (Kim et al. 2015) with '--max-intronlen 500' and parsed output files with SAMtools v1.9 (Li et
715 al. 2009) and BEDtools v2.25.0 (Quinlan and Hall 2010). Read count tables were generated
716 using ballgown (Frazee et al. 2015). Normalized expression was calculated as transcripts per
717 million (TPM) and transcripts at TPM < 1 were filtered prior to further analysis using R v4.1.2
718 (R Core Team 2018). We next used TCseq (Wu and Gu 2022) to cluster transcripts
719 (lncRNAs, mRNAs, and TEs) according to their time-course specific expression patterns. For
720 identifying co-expression connection networks, we further used WGCNA with a soft threshold
721 of 8 (Langfelder and Horvath 2008). Then, the unsigned adjacency was calculated via
722 Pearson correlation to assign transcripts into putative co-expression modules of at least 10
723 transcripts. The module-trait correlation was calculated with infection time points as traits.
724 Network visualization was done using Cytoscape v3.9.1 (Shannon et al. 2003). Functional
725 enrichment of mRNA gene sets was performed using gene ontology (GO) terms with the web
726 tool ShinyGO v0.77 (Ge et al. 2020); GO terms were summarized by using REVIGO (Supek
727 et al. 2011).
728
729

Acknowledgements

Conflict of Interest

The authors declare no competing financial and nonfinancial interests.

Data availability

All raw RNA sequencing data generated in this study are deposited at https://www.ncbi.nlm.nih.gov/sra under BioProject ID PRJNA835302.

Funding

This study was funded under the Excellence Strategy of the Federal Government and the Länder via the RWTH Aachen Exploratory Research Space (ERS) [RWTH start-up grant StUpPD362-20 to S.K.] and by the Deutsche Forschungsgemeinschaft (DFG, German Research Foundation) project number 274444799 [grant 861/14-2 awarded to R.P.] in the context of the DFG-funded priority program SPP1819 “Rapid evolutionary adaptation – potential and constraints”.

Acknowledgments

We are grateful to Xinyi Liu, Marion Müller, and Ralph Hückelhoven (TUM, Munich, Germany) for constructive feedback and collaboration on the TE consensus database. The analysis was performed with computing resources granted by RWTH Aachen University under project IDs rwth0146 and rwth0933.

Author contributions

S.K. conceived and designed the study; J.Q. and S.K. were responsible for experiment conception. J.Q. and F.K. collected samples for RNA isolation and performed RNA purification. M.E. performed qRT-PCRs of TEs; J.Q. analyzed the RNA-seq data, developed the lncRNA identification pipeline, and cloned selected lncRNAs. H.M.M.I. conceived and performed the alternative splicing analysis and identified lncRNA splice variants. S.K. and J.Q. drafted the figures. R.P. provided lab space and consumables, S.K. funding for the RNA-seq experiment. S.K. and J.Q. wrote the first draft of the manuscript, all authors contributed to editing. All authors read the manuscript and approved its final version.

763 ## References

764

765 Almagro Armenteros JJ, Tsirigos KD, Sønderby CK, Petersen TN, Winther O, Brunak
766 S, von Heijne G, Nielsen H. 2019. SignalP 5.0 improves signal peptide
767 predictions using deep neural networks. *Nat. Biotechnol.* 37:420–423.

768 Ariel FD, Manavella PA. 2021. When junk DNA turns functional: Transposon-derived
769 non-coding RNAs in plants. *J. Exp. Bot.* 72:4132–4143.

770 Barsoum M, Kusch S, Frantzeskakis L, Schaffrath U, Panstruga R. 2020. Ultraviolet
771 mutagenesis coupled with next-generation sequencing as a method for
772 functional interrogation of powdery mildew genomes. *Mol. Plant. Microbe*
773 *Interact.* 33:1008–1021.

774 Bindschedler LV, Panstruga R, Spanu PD. 2016. Mildew-Omics: How global
775 analyses aid the understanding of life and evolution of powdery mildews.
776 *Front. Plant Sci.* 7:123.

777 Blein T, Balzergue C, Roulé T, Gabriel M, Scalisi L, François T, Sorin C, Christ A,
778 Godon C, Delannoy E, et al. 2020. Landscape of the noncoding transcriptome
779 response of two Arabidopsis ecotypes to phosphate starvation. *Plant Physiol.*
780 183:1058–1072.

781 Bolger AM, Lohse M, Usadel B. 2014. Trimmomatic: A flexible trimmer for Illumina
782 sequence data. *Bioinformatics* 30:2114–2120.

783 Bologna NG, Voinnet O. 2014. The diversity, biogenesis, and activities of
784 endogenous silencing small RNAs in *Arabidopsis*. *Annu. Rev. Plant Biol.*
785 65:473–503.

786 Both M, Csukai M, Stumpf MPH, Spanu PD. 2005. Gene expression profiles of
787 *Blumeria graminis* indicate dynamic changes to primary metabolism during
788 development of an obligate biotrophic pathogen. *Plant Cell* 17:2107–2122.

789 Both M, Eckert SE, Csukai M, Müller E, Dimopoulos G, Spanu PD. 2005. Transcript
790 profiles of *Blumeria graminis* development during infection reveal a cluster of
791 genes that are potential virulence determinants. *Mol. Plant. Microbe Interact.*
792 18:125–133.

793 Braun U, Cook RTA. 2012. Taxonomic Manual of the Erysiphales (Powdery
794 Mildews). Utrecht, The Netherlands: CBS-KNAW Fungal Biodiversity Centre

795 Cai J, Jiang Y, Ritchie ES, Macho AP, Yu F, Wu D. 2023. Manipulation of plant
796 metabolism by pathogen effectors: More than just food. *FEMS Microbiol. Rev.*
797 47:fuad007.

798 Chénais B, Caruso A, Hiard S, Casse N. 2012. The impact of transposable elements
799 on eukaryotic genomes: From genome size increase to genetic adaptation to
800 stressful environments. *Gene* 509:7–15.

801 Cho J. 2018. Transposon-derived non-coding RNAs and their function in plants.
802 *Front. Plant Sci.* 9:600.

803 Choi G, Jeon J, Lee H, Zhou S, Lee Y-H. 2022. Genome-wide profiling of long non-
804 coding RNA of the rice blast fungus *Magnaporthe oryzae* during infection.
805 *BMC Genomics* 23:132.

806 Chuong EB, Elde NC, Feschotte C. 2017. Regulatory activities of transposable
807 elements: From conflicts to benefits. *Nat. Rev. Genet.* 18:71–86.

808 Djamei A, Schipper K, Rabe F, Ghosh A, Vincon V, Kahnt J, Osorio S, Tohge T,
809 Fernie AR, Feussner I, et al. 2011. Metabolic priming by a secreted fungal
810 effector. *Nature* 478:395–398.

811 Eddy SR. 2011. Accelerated profile HMM searches. *PLoS Comput. Biol.* 7:e1002195.

812 Fort V, Khelifi G, Hussein SMI. 2021. Long non-coding RNAs and transposable
813 elements: A functional relationship. *Biochim. Biophys. Acta BBA - Mol. Cell*
814 *Res.* 1868:118837.

815 Fouché S, Badet T, Oggenfuss U, Plissonneau C, Francisco CS, Croll D. 2020.
816 Stress-driven transposable element de-repression dynamics and virulence
817 evolution in a fungal pathogen. *Mol. Biol. Evol.* 37:221–239.

818 Fouché S, Oggenfuss U, Chanclud E, Croll D. 2021. A devil's bargain with
819 transposable elements in plant pathogens. *Trends Genet.* 38:222–230.

820 Frantzeskakis L, Kracher B, Kusch S, Yoshikawa-Maekawa M, Bauer S, Pedersen C,
821 Spanu PD, Maekawa T, Schulze-Lefert P, Panstruga R. 2018. Signatures of
822 host specialization and a recent transposable element burst in the dynamic
823 one-speed genome of the fungal barley powdery mildew pathogen. *BMC*
824 *Genomics* 19:381.

825 Frantzeskakis L, Németh MZ, Barsoum M, Kusch S, Kiss L, Takamatsu S, Panstruga
826 R. 2019. The *Parauncinula polyspora* draft genome provides insights into
827 patterns of gene erosion and genome expansion in powdery mildew fungi.
828 *mBio* 10:381.

829 Frazee AC, Pertea G, Jaffe AE, Langmead B, Salzberg SL, Leek JT. 2015. Ballgown
830 bridges the gap between transcriptome assembly and expression analysis.
831 *Nat. Biotechnol.* 33:243–246.

832 Fu L, Niu B, Zhu Z, Wu S, Li W. 2012. CD-HIT: Accelerated for clustering the next-
833 generation sequencing data. *Bioinformatics* 28:3150–3152.

834 Ge SX, Jung D, Yao R. 2020. ShinyGO: A graphical gene-set enrichment tool for
835 animals and plants. *Bioinformatics* 36:2628–2629.

836 Gebert D, Hewel C, Rosenkranz D. 2017. unitas: The universal tool for annotation of
837 small RNAs. *BMC Genomics* 18:644.

838 Gladyshev E. 2017. Repeat-induced point mutation and other genome defense
839 mechanisms in fungi. In: The Fungal Kingdom. American Society of
840 Microbiology. p. 687–699. Available from:
841 http://www.asmscience.org/content/book/10.1128/9781555819583.chap33

842 Glawe DA. 2008. The powdery mildews: A review of the world's most familiar (yet
843 poorly known) plant pathogens. *Annu. Rev. Phytopathol.* 46:27–51.

844 Goubert C, Craig RJ, Bilat AF, Peona V, Vogan AA, Protasio AV. 2022. A beginner's
845 guide to manual curation of transposable elements. *Mob. DNA* 13:7.

846 Hacquard S, Kracher B, Maekawa T, Vernaldi S, Schulze-Lefert P, van Themaat
847 EVL. 2013. Mosaic genome structure of the barley powdery mildew pathogen
848 and conservation of transcriptional programs in divergent hosts. *Proc. Natl.*
849 *Acad. Sci. U. S. A.* 110:E2219–E2228.

850 Hill R, Buggs RJA, Vu DT, Gaya E. 2022. Lifestyle transitions in fusarioid fungi are
851 frequent and lack clear genomic signatures. *Mol. Biol. Evol.* 39:msac085.

852 Hunt M, Banerjee S, Surana P, Liu M, Fuerst G, Mathioni S, Meyers BC, Nettleton D,
853 Wise RP. 2019. Small RNA discovery in the interaction between barley and
854 the powdery mildew pathogen. *BMC Genomics* 20:610.

855 Jampala P, Garhewal A, Lodha M. 2021. Functions of long non-coding RNA in
856 *Arabidopsis thaliana*. *Plant Signal. Behav.* 16:1925440.

857 Johnson R, Guigó R. 2014. The RIDL hypothesis: Transposable elements as
858 functional domains of long noncoding RNAs. *RNA* 20:959–976.

859 Jones P, Binns D, Chang H-Y, Fraser M, Li W, McAnulla C, McWilliam H, Maslen J,
860 Mitchell A, Nuka G, et al. 2014. InterProScan 5: Genome-scale protein
861 function classification. *Bioinformatics* 30:1236–1240.

862 Kalem MC, Panepinto JC. 2022. Long non-coding RNAs in *Cryptococcus*
863 *neoformans*: Insights into fungal pathogenesis. *Front. Cell. Infect. Microbiol.*
864 12:858317.

865 Kalvari I, Argasinska J, Quinones-Olvera N, Nawrocki EP, Rivas E, Eddy SR,
866 Bateman A, Finn RD, Petrov AI. 2018. Rfam 13.0: Shifting to a genome-centric
867 resource for non-coding RNA families. *Nucleic Acids Res.* 46:D335–D342.

868 Kalwa M, Hänzelmann S, Otto S, Kuo C-C, Franzen J, Joussen S, Fernandez-
869 Rebollo E, Rath B, Koch C, Hofmann A, et al. 2016. The lncRNA HOTAIR
870 impacts on mesenchymal stem cells *via* triple helix formation. *Nucleic Acids*
871 *Res.* 44:10631–10643.

872 Kang Y-J, Yang D-C, Kong L, Hou M, Meng Y-Q, Wei L, Gao G. 2017. CPC2: A fast
873 and accurate coding potential calculator based on sequence intrinsic features.
874 *Nucleic Acids Res.* 45:W12–W16.

875 Kapusta A, Kronenberg Z, Lynch VJ, Zhuo X, Ramsay L, Bourque G, Yandell M,
876 Feschotte C. 2013. Transposable elements are major contributors to the
877 origin, diversification, and regulation of vertebrate long noncoding RNAs. *PLoS*
878 *Genet.* 9:e1003470.

879 Kim D, Langmead B, Salzberg SL. 2015. HISAT: A fast spliced aligner with low
880 memory requirements. *Nat. Methods* 12:357–360.

881 Kopp F, Mendell JT. 2018. Functional classification and experimental dissection of
882 long noncoding RNAs. *Cell* 172:393–407.

883 Krogh A, Larsson B, von Heijne G, Sonnhammer ELL. 2001. Predicting
884 transmembrane protein topology with a hidden markov model: application to
885 complete genomes. *J. Mol. Biol.* 305:567–580.

886 Kusch S, Ahmadinejad N, Panstruga R, Kuhn H. 2014. *In silico* analysis of the core
887 signaling proteome from the barley powdery mildew pathogen (*Blumeria*
888 *graminis* f.sp. *hordei*). *BMC Genomics* 15:843.

889 Kusch S, Frantzeskakis L, Thieron H, Panstruga R. 2018. Small RNAs from cereal
890 powdery mildew pathogens may target host plant genes. *Fungal Biol.*
891 122:1050–1063.

892 Kusch S, Larrouy J, Ibrahim HMM, Mounichetty S, Gasset N, Navaud O, Mbengue M,
893 Zanchetta C, Lopez-Roques C, Donnadieu C, et al. 2022. Transcriptional
894 response to host chemical cues underpins the expansion of host range in a
895 fungal plant pathogen lineage. *ISME J.* 16:138–148.

896 Kusch S, Qian J, Loos A, Kümmel F, Spanu PD, Panstruga R. 2023. Long-term and
897 rapid evolution in powdery mildew fungi. *Mol. Ecol.*:mec.16909.

898 Kusch S, Singh M, Thieron H, Spanu PD, Panstruga R. 2023. Site-specific analysis
899 reveals candidate cross-kingdom small RNAs, tRNA and rRNA fragments, and

900 signs of fungal RNA phasing in the barley–powdery mildew interaction. *Mol.*
901 *Plant Pathol.* 24:570–587.

902 Labbé J, Murat C, Morin E, Tuskan GA, Le Tacon F, Martin F. 2012. Characterization
903 of transposable elements in the ectomycorrhizal fungus *Laccaria bicolor*. *PLoS*
904 *ONE* 7:e40197.

905 Lanciano S, Cristofari G. 2020. Measuring and interpreting transposable element
906 expression. *Nat. Rev. Genet.* 21:721–736.

907 Langfelder P, Horvath S. 2008. WGCNA: An R package for weighted correlation
908 network analysis. *BMC Bioinformatics* 9:559.

909 Langmead B, Salzberg SL. 2012. Fast gapped-read alignment with Bowtie 2. *Nat.*
910 *Methods* 9:357–359.

911 Lee E, Helt GA, Reese JT, Munoz-Torres MC, Childers CP, Buels RM, Stein LD,
912 Holmes IH, Elsik CG, Lewis SE. 2013. Web Apollo: A web-based genomic
913 annotation editing platform. *Genome Biol.* 14:R93.

914 Li H, Handsaker B, Wysoker A, Fennell T, Ruan J, Homer N, Marth G, Abecasis G,
915 Durbin R. 2009. The Sequence Alignment/Map format and SAMtools.
916 *Bioinformatics* 25:2078–2079.

917 Li J, Liu X, Yin Z, Hu Z, Zhang K-Q. 2021. An overview on identification and
918 regulatory mechanisms of long non-coding RNAs in fungi. *Front. Microbiol.*
919 12:638617.

920 Li L, Collier B, Spanu P. 2019. Isolation of powdery mildew haustoria from infected
921 barley. *Bio-Protoc.* 9:e3299.

922 Liao W, Nielsen ME, Pedersen C, Xie W, Thordal-Christensen H. 2023. Barley
923 endosomal MONENSIN SENSITIVITY1 is a target of the powdery mildew
924 effector CSEP0162 and plays a role in plant immunity. *J. Exp. Bot.* 74:118–
925 129.

926 Livak KJ, Schmittgen TD. 2001. Analysis of relative gene expression data using real-
927 time quantitative PCR and the 2−ΔΔCT method. *Methods* 25:402–408.

928 Lo Presti L, Lanver D, Schweizer G, Tanaka S, Liang L, Tollot M, Zuccaro A,
929 Reissmann S, Kahmann R. 2015. Fungal effectors and plant susceptibility.
930 *Annu. Rev. Plant Biol.* 66:513–545.

931 Lv Y, Hu F, Zhou Y, Wu F, Gaut BS. 2019. Maize transposable elements contribute
932 to long non-coding RNAs that are regulatory hubs for abiotic stress response.
933 *BMC Genomics* 20:864.

934 Mascher M, Wicker T, Jenkins J, Plott C, Lux T, Koh CS, Ens J, Gundlach H, Boston
935 LB, Tulpová Z, et al. 2021. Long-read sequence assembly: A technical
936 evaluation in barley. *Plant Cell* 33:1888–1906.

937 Mattick JS, Amaral PP, Carninci P, Carpenter S, Chang HY, Chen L-L, Chen R, Dean
938 C, Dinger ME, Fitzgerald KA, et al. 2023. Long non-coding RNAs: Definitions,
939 functions, challenges and recommendations. *Nat. Rev. Mol. Cell Biol.* 24:430–
940 447.

941 Müller MC, Praz CR, Sotiropoulos AG, Menardo F, Kunz L, Schudel S, Oberhänsli S,
942 Poretti M, Wehrli A, Bourras S, et al. 2019. A chromosome-scale genome
943 assembly reveals a highly dynamic effector repertoire of wheat powdery
944 mildew. *New Phytol.* 221:2176–2189.

945 Nicolás FE, Ruiz-Vázquez RM. 2013. Functional diversity of RNAi-associated sRNAs
946 in fungi. *Int. J. Mol. Sci.* 14:15348–15360.

947 Nottensteiner M, Zechmann B, McCollum C, Hückelhoven R. 2018. A barley powdery
948 mildew fungus non-autonomous retrotransposon encodes a peptide that
949 supports penetration success on barley. *J. Exp. Bot.* 69:3745–3758.

950 O'Connell RJ, Thon MR, Hacquard S, Amyotte SG, Kleemann J, Torres MF, Damm
951 U, Buiate EA, Epstein L, Alkan N, et al. 2012. Lifestyle transitions in plant
952 pathogenic *Colletotrichum* fungi deciphered by genome and transcriptome
953 analyses. *Nat. Genet.* 44:1060–1065.

954 Ou S, Su W, Liao Y, Chougule K, Agda JRA, Hellinga AJ, Lugo CSB, Elliott TA, Ware
955 D, Peterson T, et al. 2019. Benchmarking transposable element annotation
956 methods for creation of a streamlined, comprehensive pipeline. *Genome Biol.*
957 20:275.

958 Pedersen C, van Themaat EVL, McGuffin LJ, Abbott JC, Burgis TA, Barton G,
959 Bindschedler LV, Lu X, Maekawa T, Weßling R, et al. 2012. Structure and
960 evolution of barley powdery mildew effector candidates. *BMC Genomics*
961 13:694.

962 Pennington HG, Li L, Spanu PD. 2015. Identification and selection of normalization
963 controls for quantitative transcript analysis in *Blumeria graminis*. *Mol. Plant*
964 *Pathol.* 17:625–633.

965 Pertea G, Pertea M. 2020. GFF Utilities: GffRead and GffCompare. *F1000Research*
966 9:304.

967 Pertea M, Pertea GM, Antonescu CM, Chang T-C, Mendell JT, Salzberg SL. 2015.
968 StringTie enables improved reconstruction of a transcriptome from RNA-seq
969 reads. *Nat. Biotechnol.* 33:290–295.

970 Potter SC, Luciani A, Eddy SR, Park Y, Lopez R, Finn RD. 2018. HMMER web
971 server: 2018 update. *Nucleic Acids Res.* 46:W200–W204.

972 Quinlan AR, Hall IM. 2010. BEDTools: A flexible suite of utilities for comparing
973 genomic features. *Bioinformatics* 26:841–842.

974 Quinn JJ, Chang HY. 2015. Unique features of long non-coding RNA biogenesis and
975 function. *Nat. Rev. Genet.* 17:47–62.

976 R Core Team. 2018. R: A language and environment for statistical computing. *R*
977 *Found. Stat. Comput. Vienna Austria* [Internet]. Available from: http://www.r-
978 project.org/

979 Robinson JT, Thorvaldsdóttir H, Winckler W, Guttman M, Lander ES, Getz G,
980 Mesirov JP. 2011. Integrative Genomics Viewer. *Nat. Biotechnol.* 29:24–26.

981 Sabelleck B, Panstruga R. 2018. Novel jack-in-the-box effector of the barley powdery
982 mildew pathogen? *J. Exp. Bot.* 69:3511–3514.

983 Saur IML, Panstruga R, Schulze-Lefert P. 2021. NOD-like receptor-mediated plant
984 immunity: From structure to cell death. *Nat. Rev. Immunol.* 21:305–318.

985 Schmidt SM, Kuhn H, Micali C, Liller C, Kwaaitaal M, Panstruga R. 2014. Interaction
986 of a *Blumeria graminis* f. sp. *hordei* effector candidate with a barley ARF-GAP
987 suggests that host vesicle trafficking is a fungal pathogenicity target: *Blumeria*
988 *graminis* effector candidates. *Mol. Plant Pathol.* 15:535–549.

989 Shannon P, Markiel A, Ozier O, Baliga NS, Wang JT, Ramage D, Amin N,
990 Schwikowski B, Ideker T. 2003. Cytoscape: A software environment for
991 integrated models of biomolecular interaction networks. *Genome Res.*
992 13:2498–2504.

993 Slotkin RK, Martienssen R. 2007. Transposable elements and the epigenetic
994 regulation of the genome. *Nat. Rev. Genet.* 8:272–285.

995 Smit AFA, Hubley R, Green P. 2016. Masker Open-4.0. 2013-2015. Available from:
996 http://www.repeatmasker.org

997 Spanu PD. 2017. Cereal immunity against powdery mildews targets RNase-Like
998 Proteins associated with Haustoria (RALPH) effectors evolved from a common
999 ancestral gene. *New Phytol.* 213:969–971.

1000 Spanu PD, Abbott JC, Amselem J, Burgis TA, Soanes DM, Stüber K, van Themaat
1001 EVL, Brown JKM, Butcher SA, Gurr SJ, et al. 2010. Genome expansion and
1002 gene loss in powdery mildew fungi reveal tradeoffs in extreme parasitism.
1003 *Science* 330:1543–1546.

1004 Stergiopoulos I, De Wit PJGM. 2009. Fungal effector proteins. *Annu. Rev.*
1005 *Phytopathol.* 47:233–263.

1006 Supek F, Bošnjak M, Škunca N, Šmuc T. 2011. REVIGO summarizes and visualizes
1007 long lists of Gene Ontology terms. *PLoS ONE* 6:e21800.

1008 Till P, Mach RL, Mach-Aigner AR. 2018. A current view on long noncoding RNAs in
1009 yeast and filamentous fungi. *Appl. Microbiol. Biotechnol.* 102:7319–7331.

1010 Till P, Pucher ME, Mach RL, Mach-Aigner AR. 2018. A long noncoding RNA
1011 promotes cellulase expression in *Trichoderma reesei*. *Biotechnol. Biofuels*
1012 11:78.

1013 Ulitsky I, Bartel DP. 2013. lincRNAs: Genomics, evolution, and mechanisms. *Cell*
1014 154:26–46.

1015 Wang D, Qu Z, Yang L, Zhang Q, Liu Z, Do T, Adelson DL, Wang Z, Searle I, Zhu J.
1016 2017. Transposable elements (TEs) contribute to stress-related long intergenic
1017 noncoding RNAs in plants. *Plant J.* 90:133–146.

1018 Wang Yang, Ye W, Wang Yuanchao. 2018. Genome-wide identification of long non-
1019 coding RNAs suggests a potential association with effector gene transcription
1020 in *Phytophthora sojae*. *Mol. Plant Pathol.* 19:2177–2186.

1021 Wang Z, Jiang Y, Wu H, Xie X, Huang B. 2019. Genome-wide identification and
1022 functional prediction of long non-coding RNAs involved in the heat stress
1023 response in *Metarhizium robertsii*. *Front. Microbiol.* 10:2336.

1024 Wicker T, Sabot F, Hua-Van A, Bennetzen JL, Capy P, Chalhoub B, Flavell A, Leroy
1025 P, Morgante M, Panaud O, et al. 2007. A unified classification system for
1026 eukaryotic transposable elements. *Nat. Rev. Genet.* 8:973–982.

1027 Wu M, Gu L. 2022. TCseq: Time course sequencing data analysis. :R package
1028 version 1.20.0.

1029 Wucher V, Legeai F, Hédan B, Rizk G, Lagoutte L, Leeb T, Jagannathan V, Cadieu
1030 E, David A, Lohi H, et al. 2017. FEELnc: A tool for long non-coding RNA
1031 annotation and its application to the dog transcriptome. *Nucleic Acids Res.*
1032 45:e57.

1033 Zhang X, Wang W, Zhu W, Dong J, Cheng Y, Yin Z, Shen F. 2019. Mechanisms and
1034 functions of long non-coding RNAs at multiple regulatory levels. *Int. J. Mol.*
1035 *Sci.* 20:5573.

1036 Zhao X-Y, Lin JD. 2015. Long noncoding RNAs: A new regulatory code in metabolic
1037 control. *Trends Biochem. Sci.* 40:586–596.

1040 ## Supplementary Data

1041

1042 **Supplementary Figure 1. Integrated pipeline for high-quality genome-wide TE**
1043 **annotation.** We initially detected transposable elements (TEs) the genome assembly of
1044 *B. hordei* isolate DH14 (Frantzeskakis et al. 2018) using the extensive *de novo* annotator
1045 (EDTA) pipeline (Ou et al. 2019), which enables de novo discovery of long terminal repeat
1046 (LTR), terminal inverted repeat (TIR), and DNA helitron TEs. In parallel, we queried the
1047 genome for TE elements using the *Blumeria* TE consensus sequences from RepBase
1048 v20181026; short interspersed nuclear element (SINE) TE sequences were extracted from
1049 GenBank accessions X86077.1 (*Eg-R1*) and Z21962.1 (*Egh24*). Similar TE sequences were
1050 merged with CD-HIT-EST (Fu et al. 2012). Then, we generated the consensus repeat
1051 database via multiple sequence alignment and manual curation of consensus TEs (Goubert
1052 et al. 2022). Genome-wide re-annotation of TEs in the genome assembly of *B. hordei* isolate
1053 DH14 (Frantzeskakis et al. 2018) was done with RepeatMasker (Smit et al. 2016) using the
1054 repeat consensus library as database (**Table 1**; **Supplementary Table 2**).

1055

1056 **Supplementary Figure 2. Integrated pipeline for high-quality genome-wide TE**
1057 **annotation.**
1058 We performed quantitative reverse transcriptase-polymerase chain reaction (qRT-PCR)
1059 analysis of eleven selected TE families. The dot plots show the relative transcript abundance
1060 (according to $\Delta\Delta^{CT}$ analysis; y-axis) of the respective TE family, indicated on the top of each
1061 panel, in *B. hordei* isolate $K1_{AC}$ at seven time points of host infection (hours post inoculation
1062 (hpi); x-axis). TE transcript levels were normalized to *B. hordei GAPDH* (*BLGH_00691*); we
1063 conducted three independent replicates ($n = 3$) consisting of three technical replicates each.
1064 The shades of green indicate the replicate each data point belongs to; the black bar shows
1065 the median.

1066

1067 **Supplementary Figure 3. *H. vulgare* displays infection stage-dependent expression**
1068 **patterns of coding genes upon infection with *B. hordei*.**
1069 (**A**) We clustered time-resolved coding gene expression patterns in the host *H. vulgare* cv.
1070 'Margret' upon infection with *B. hordei* $K1_{AC}$ using TCseq (Wu and Gu 2022). The RNA-seq
1071 data was mapped to the *H. vulgare* cv. 'Morex' reference genome (Mascher et al. 2021)
1072 using HISAT2 (Kim et al. 2015) with '--max-intronlen 500' and parsed output using SAMtools
1073 v1.9 (Li et al. 2009) and BEDtools v2.25.0 (Quinlan and Hall 2010). The lines represent
1074 single transcripts; the color shade denotes the cluster membership by Spearman correlation
1075 (the darker the shade of blue, the higher the correlation *R* with the respective expression
1076 cluster according to the color scheme). The numbers at the bottom-right of each plot

1077 indicates the number of genes that made up each of the time course clusters. The x-axis
1078 denotes the time points of infection in hours post inoculation (hpi; **Figure 1A**), which were
1079 0 hpi (conidiospore germination), 6 hpi (appressorium formation), 18 hpi (host cell
1080 penetration), 24 hpi (haustorium formation), 72 hpi (epiphytic colonization), and 120 hpi
1081 (conidiogenesis). The y-axis indicates the relative z-score based on reads per kb of transcript
1082 per million mapped reads (RPKM). (**B**) We performed gene ontology (GO) enrichment
1083 analysis for the *H. vulgare* coding genes from each cluster (**A**) using ShinyGO v0.77 (Ge et
1084 al. 2020) accessed online at http://bioinformatics.sdstate.edu/go/, and summarized GO terms
1085 with REVIGO (Supek et al. 2011). The dot plot displays the fold enrichment of functional
1086 terms compared to the full set of genes of *H. vulgare* cv. 'Morex' (dot size); the fill color
1087 indicates the $-\text{Log}_{10}$(FDR-adjusted enrichment *p* value) according to the color scheme on the
1088 right. The GO term accessions are indicated on the x-axis; colored dots denote summarizing
1089 GO descriptions indicated in the legend (top-right). The respective co-expression cluster (**A**)
1090 is indicated on the y-axis.
1091
1092 **Supplementary Figure 4. Co-expression analysis of TEs, coding genes, and lncRNAs**
1093 **in *B. hordei*.** (**A**) We built co-regulation networks using WGCNA (Langfelder and Horvath
1094 2008) using the time course expression data of *B. hordei* coding genes (mRNAs), lncRNAs,
1095 and consensus TEs. The time points of infection were 0 hpi (spore germination), 6 hpi
1096 (appressorium formation), 18 hpi (early primary haustorium), 24 hpi (mature primary
1097 haustorium), 72 hpi (host colonization), and 120 hpi (conidia formation). The twenty identified
1098 co-expression clusters are indicated on the y-axis and the time points on the x-axis. The
1099 Pearson correlation of each cluster with the respective time point is shown on a scale from
1100 green to red, indicating negative to positive correlation. The exact Pearson correlation value
1101 and the *p* value are shown for each cluster and time point. (**B**) The colored circles indicate
1102 transcripts and lines significant correlation between two transcripts. The circles are colored
1103 according to the WGCNA-assigned cluster colors (**A**). The clusters correspond to the clusters
1104 in **Figure 6**.
1105
1106
1107 **Supplementary Table 1.** General statistics of the RNA sequencing datasets generated for
1108 this study.
1109 **Supplementary Table 2**. Transposable element composition in the *B. hordei* DH14 genome
1110 based on our manual transposon database.
1111 **Supplementary Table 3**. Functional annotations of the proteins encoded by the 43 coding
1112 genes newly discovered in the *B. hordei* genome
1113 **Supplementary Table 4**. Transcripts per million expression values for mRNAs and lncRNAs
1114 of *B. hordei* $K1_{AC}$ during infection of *H. vulgare* cv. 'Margret'.

1115 **Supplementary Table 5**. Gene ontology (GO) enrichment of *B. hordei* mRNAs induced at
1116 specific time points of infection.
1117 **Supplementary Table 6**. Gene ontology (GO) enrichment of *H. vulgare* mRNAs induced at
1118 specific time points of infection.
1119 **Supplementary Table 7**. Pearson correlation table for co-regulation of lncRNAs with mRNAs
1120 in *B. hordei*.
1121 **Supplementary Table 8**. Pearson correlation table for co-regulation of lncRNAs with
1122 consensus TEs in *B. hordei*.
1123 **Supplementary Table 9**. List of oligonucleotides used for PCR amplification and qRT-PCR.
1124